Lawrence Berkeley National Laboratory
LBL Dissertations

Title
NUCLEAR INTERACTIONS OF ANTIPROTONS

Permalink
https://escholarship.org/uc/item/6206007b

Author
Keller, Donald V.

Publication Date
1957-07-15

Thesis/dissertation

eScholarship.org Powered by the California Digital Library
University of California

UCRL 3855
Copy 2

UNIVERSITY OF CALIFORNIA

Ernest O. Lawrence

Radiation Laboratory

TWO-WEEK LOAN COPY

This is a Library Circulating Copy which may be borrowed for two weeks. For a personal retention copy, call Tech. Info. Division, Ext. 5545

BERKELEY, CALIFORNIA

DISCLAIMER

This document was prepared as an account of work sponsored by the United States Government. While this document is believed to contain correct information, neither the United States Government nor any agency thereof, nor the Regents of the University of California, nor any of their employees, makes any warranty, express or implied, or assumes any legal responsibility for the accuracy, completeness, or usefulness of any information, apparatus, product, or process disclosed, or represents that its use would not infringe privately owned rights. Reference herein to any specific commercial product, process, or service by its trade name, trademark, manufacturer, or otherwise, does not necessarily constitute or imply its endorsement, recommendation, or favoring by the United States Government or any agency thereof, or the Regents of the University of California. The views and opinions of authors expressed herein do not necessarily state or reflect those of the United States Government or any agency thereof or the Regents of the University of California.

UCRL-3855

UNIVERSITY OF CALIFORNIA
Radiation Laboratory
Berkeley, California

Contract No. W-7405-eng-48

NUCLEAR INTERACTIONS OF ANTIPROTONS

Donald V. Keller

(Thesis)

July 15, 1957

Printed for the U. S. Atomic Energy Commission

NUCLEAR INTERACTIONS OF ANTIPROTONS

Contents

Abstract 3

Introduction 4

I. Run I. Antiproton Interactions in Beryllium and Copper

A. Introduction 6

B. The Antiproton Beam 7

C. Experimental 7

D. Results 13

E. Discussion 16

II. Run II. Antiproton Interactions with Nucleons and Complex Nuclei

A. Introduction 17

B. The Antiproton Beam 17

C. Experimental 23

1. Attenuators 23

2. Geometry 25

3. Counters 26

4. Electronics and Photography 29

5. Procedure 31

D. Reduction of Data 32

1. Film Reading 32

2. IBM-650 Analysis 35

3. Notation 35

4. Interpretation of C^{**} Pulses 36

E. Antiproton-Nucleon Cross Sections 46

1. Formulas and Results 46

2. Errors 48

3. Shielding Corrections 51

4. Total Antiproton-Nucleon Cross Sections 54

5. Conclusions 56

F. Cross Sections for Antiprotons on Complex-Nuclei . . . 56

1. Results 56

NUCLEAR INTERACTIONS OF ANTIPROTONS

Donald V. Keller

Radiation Laboratory
University of California
Berkeley, California

July 15, 1957

ABSTRACT

Attenuation and total annihilation cross sections were measured for 497-Mev antiprotons incident on H_2O, D_2O, O_2, Be, Cu, Ag, and Pb. In addition, cross sections for positive protons were measured for all of the above materials under identical experimental conditions. The H_2O, D_2O, and O_2 results were subtracted to give the $\bar{p}p$, $\bar{p}n$, and $\bar{p}d$ attenuation and total annihilation cross sections. Within the 10% statistical accuracy of this experiment, and within the accuracy of a large correction due to the fact that in the deuteron the neutron is hidden partly by the proton, the $\bar{p}p$ and $\bar{p}n$ attenuation cross sections are the same, both being about 4 times larger than the pp cross section at the energy involved. The $\bar{p}p$ and $\bar{p}n$ total annihilation cross sections are also equal, within the experimental errors, and represent approximately 80% of the total attenuation cross sections. The poor-geometry cross sections for O_2, Cu, Ag, and Pb were extrapolated to zero solid angle to obtain the total inelastic cross sections. The ratio of the total inelastic cross section for antiprotons to that for protons seems to decrease as the atomic number Z increases (1.74 for O_2, 1.44 for Cu, 1.39 for Ag) indicating that the difference between the antiproton and proton cross sections on complex nuclei may be due to the interactions of the antiprotons with nucleons near the surface of the nucleus. The ratio of the annihilation cross section to the total inelastic cross section is approximately 0.75 for the four elements investigated and seems to increase with increasing Z.

INTRODUCTION

Immediately following the discovery of the antiproton in 1955 at the Berkeley Bevatron,[1] experiments were begun to study the interactions of this new particle with ordinary matter. The first step in this direction was a counter experiment[2] (Run I) performed to measure the attenuation of antiprotons in two elements, copper and beryllium. This preliminary experiment showed two striking features of the interaction of high-energy antiprotons with complex nuclei: an attenuation cross section that was approximately twice as large as that for positive protons, and a large probability for annihilation with one of the nucleons of the nucleus. Several other experiments, involving both counters[3, 4] and emulsions,[5, 6, 7] have been performed; all have indicated general agreement with these first results.

Moreover, a recent counter experiment[4] was completed which measured the total cross section for the antiproton-proton interaction at several antiproton energies. The result is a total cross section of about 100 mb for the energies investigated. This cross section is very startling when compared to the total pp cross section at the same energy (500 Mev) of 25 mb. In the above experiment no attempt was made to determine the $\bar{p}p$ annihilation cross section. The measurement of this annihilation cross section was, therefore, one of the primary objectives of our experiment. We wished to see whether or not the surprisingly large total cross section was a direct result of the annihilation process. In addition, it was desirable to know whether similar results obtained for the antiproton-neutron interaction.

In order to measure the $\bar{p}n$ cross sections, it is necessary to perform a subtraction experiment--in our case D_2O-H_2O, and make substantial corrections for the obscuration of the neutron by the proton in deuterium. We decided to study the $\bar{p}p$ interaction by the same method rather than by measuring the transmission of antiprotons through liquid hydrogen as was done in reference 4. While the method chosen yields less accurate results for the total cross section, it

I. RUN I: ANTIPROTON INTERACTIONS IN BERYLLIUM AND COPPER

A. Introduction

In this section we describe a counter experiment performed to measure the antiproton attenuation both in copper and in beryllium.

Antiprotons, certified as to their nature by the system of counters described in the following section, were allowed to impinge on an absorber. Two additional counters were used to determine how many passed through the absorber. One of these counters was a scintillation counter that was sensitive to all charged particles passing through it. These charged particles were (a) "pass-through" antiprotons--by which we mean those that failed to have a nuclear interaction, or at most were scattered through an angle smaller than θ_c (where θ_c is the half angle subtended by the counter at the center of the absorber)--and (b) charged secondaries resulting from the annihilation of an antiproton with a nucleon. In order to determine the cross section correctly, we had to recognize these charged secondaries, because they would otherwise simulate pass-through antiprotons and thereby cause the measured cross sections to be too small. For this purpose, we used as a "guard" counter a water Cerenkov counter that counted only those particles with a velocity greater than $\beta = 0.75$ ($\beta = \frac{v}{c}$). Because the incident antiprotons had a velocity of $\beta = 0.75$ before entering the attenuator, they were not counted in this guard counter. Therefore, in order that a pulse in the detector counter will represent a pass-through antiproton, we have added the stipulation that there must be no count in the Cerenkov guard counter.

The antiproton cross sections were compared with those for protons by an experiment in which the currents in the analyzing magnets (M1, M2) and focusing magnets (Q1, Q2) were reversed. It was also necessary to change the position of the target slightly in order to allow the protons to pass through the fringing field of the Bevatron into the orbit defined by the magnets and counters. For these runs the Bevatron

allows a determination of the annihilation cross sections, as described below. This involves one additional measurement; namely, that of the attenuation of antiprotons by liquid oxygen. The experiment (Run II), therefore, consisted of measuring the transmission of antiprotons through three materials--D_2O, H_2O, and O_2--and performing subtractions to gain information concerning the $\bar{p}p$ and $\bar{p}n$ interactions. Because the annihilation process proceeds primarily through the production of mesons,[7] this method affords a convenient way of measuring directly the annihilation cross section for these three materials. There will nearly always be at least one charged annihilation meson produced that is fast enough to radiate Cerenkov light in D_2O, H_2O, or O_2. The procedure was to look directly at the attenuator material with phototubes, thus detecting the Cerenkov light emitted by these annihilation mesons.

We decided also to extend the previous experiments with antiprotons on complex nuclei to include measurements with copper, silver, and lead. The plan was to obtain both reaction (or total inelastic) and total annihilation cross sections for these substances--the former by measuring poor-geometry cross sections at two different cut-off angles and extrapolating to zero solid angle, and the latter by a method similar to that described in the previous paragraph. The target materials were surrounded by a colorless liquid in which the Cerenkov light from the annihilation mesons was detected by phototubes.

In Part I of this report we will describe briefly the initial experiment mentioned above (Run I) in which cross sections for antiprotons on beryllium and copper were measured. Part II of this report treats the experiments of Run II on the interactions of antiprotons with nucleons and antiprotons with complex nuclei. The experimental details of Run II are discussedin Section II-C, and the data-reduction methods are discussed in Section II-D. Section II-E contains the antiproton-nucleon results and discussion, and Section II-F contains the results of the measurements of interactions of antiprotons with complex nuclei.

internal beam was accelerated to 1.1 Bev. There was no meson contamination of this 1.19-Bev/c proton beam because mesons of this momentum could not be produced by 1.1-Bev protons.

B. The Antiproton Beam

The antiproton beam used in this experiment was the same beam in which antiprotons were discovered,[1] and is pictured schematically in Fig. 1. M1 and M2 are bending magnets to aid in the separation of antiprotons from the huge pion background. Q1 and Q2 are magnetic quadrupole focusing lenses. S1, S2, and S3 are ordinary scintillation counters, and C1 and C2 are Cerenkov counters. These five counters comprise the antiproton detecting apparatus, and the antiprotons passing through S3 are then allowed to impinge on a target. The energy of the antiproton beam at S3 was 497± 10 Mev, and the beam had a root-mean-square angular divergence of ± 3^{o}, which was due mainly to multiple Coulomb scattering in counters C1 and C2.

C. Experimental

Table I gives the specifications of the three counters S3, C3, and S4. S3 and S4 were plastic scintillation counters, whereas C3 was the water Cerenkov guard counter mentioned earlier. At the suggestion of Dr. Bruce Cork of this laboratory, C3 was placed directly behind the attenuator, rather than behind the detector S4, thereby subtending a larger solid angle at the absorber and thus having a better efficiency for counting annihilation events. However, by placing counter C3 between counters S3 and S4, we increased the amount of absorbing material through which the beam had to pass. The copper equivalent of counter C3 (water plus tube and base) was about 22 g/cm^2 Cu. In order to correct for the attenuation in this additional absorbing material, it was necessary to take data with the primary attenuator out as well as in place. It should also be noted that it was very unlikely that an annihilation pion produced in the primary absorber could

traverse the water without having sufficient energy to emit Cerenkov radiation in so doing.

The three pulses from counters S3, C3, and S4 were displayed on an oscilloscope trace and photographically recorded. Another camera was simultaneously photographing the pulses from counters S1, S2, and C1. These latter traces were used only for recognition of the antiprotons (as discussed in Reference 1). The traces of the two films were then correlated and the S3, C3, and S4 pulses recorded for antiproton traces. All double sweeps (two or more sweeps sometimes occured within the 50 msec duration of the beam pulse) were discarded because their inclusion might introduce a systematic error.

Table I

Counter Specifications: Run I

Counter	Type	Diameter (in.)	Thickness (in.)	Remarks
S3	Plastic Scintillator	4	1	
S4	Plastic Scintillator	7	0.5	Used only in copper experiment
S4	Plastic Scintillator	13	1	Used only in beryllium experiment
C3	Water Cerenkov	7.5	3.5	

The extremely low counting rate (an average of one antiproton every 15 min) limited our measurements to only two elements; we have chosen copper and beryllium. The thickness of the copper absorber was 68 g/cm^2, the beryllium 37.5 g/cm^2.

A schematic drawing of the experimental arrangement is shown in Fig. 2 for the copper geometry, and in Fig. 3, for the beryllium geometry.

The angle subtended by the pass-through counter S4 at the center of the attenuator is conventionally called the cutoff angle, θ_c. However, the divergence of the incident beam and the thickness of the

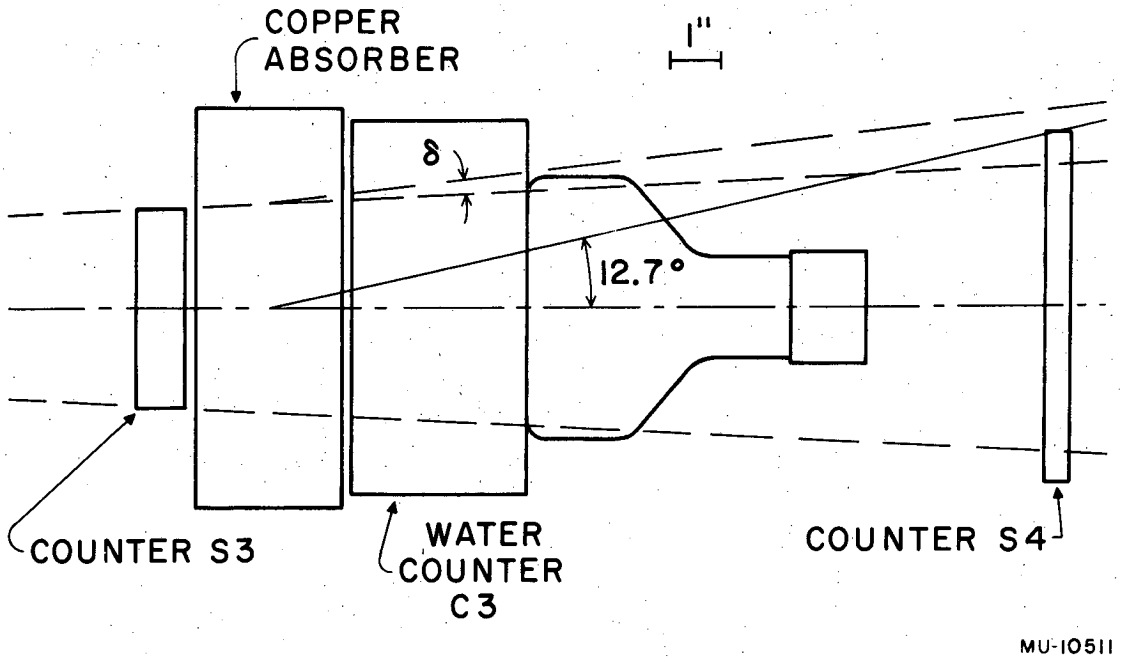


Fig. 2. Schematic diagram of geometry for copper measurement, Run I.

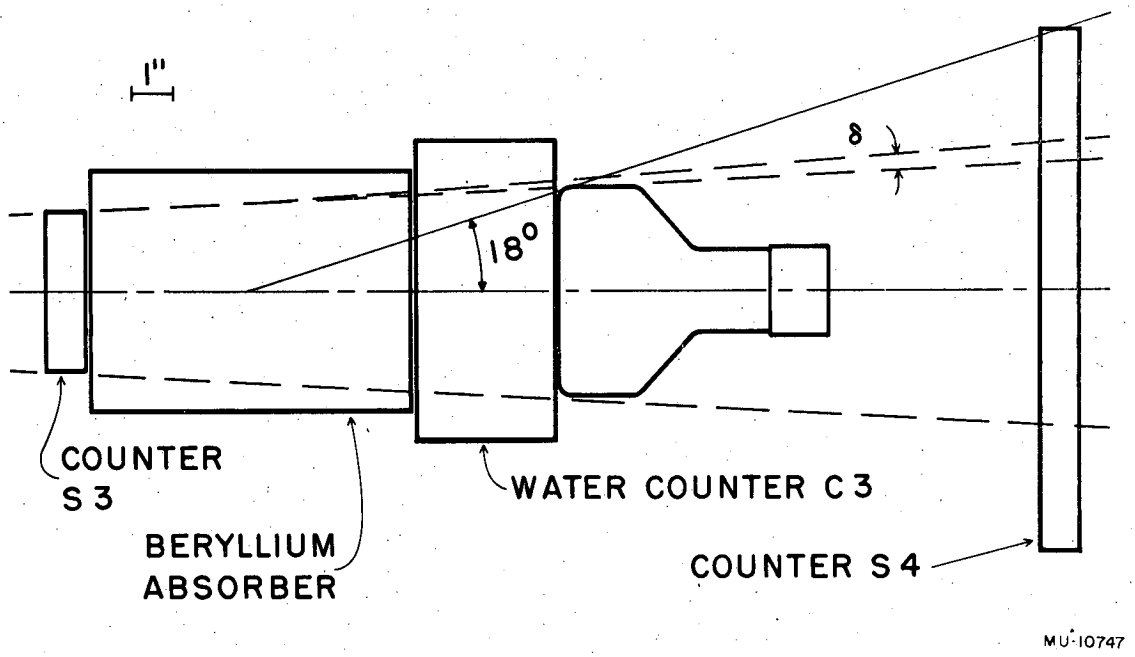


Fig. 3. Schematic diagram of geometry for beryllium measurement, Run I.

attenuators introduced an uncertainty in the real cutoff angle, especially in the copper geometry. For this reason it was desirable to choose an angle for which the cross section is not strongly dependent on θ_c. Thus, the cutoff angle was chosen larger than the angle at the first minimum of the diffraction pattern for protons, so that the detector S4 counted nearly all antiprotons that had suffered only diffraction and multiple Coulomb scattering. Hence the quoted cross sections include only negligible amounts of diffraction scattering. This has been verified by calculation. In Figs. 2 and 3, the incident divergent beam is shown with dashed lines, and the rms angle δ of multiple Coulomb scattering is indicated. The cutoff angles were $\theta_c = 12.7^\circ$ for copper and $\theta_c = 18^\circ$ for beryllium.

An incident particle must always count in S3. In the remaining two counters, C3 and S4, there are only four possible different combinations of responses. These will be labeled (C3, S4), ($\overline{C3}$, S4) (C3, $\overline{S4}$), and ($\overline{C3}$, $\overline{S4}$), where a bar indicates that the corresponding counter did not count.

For the purposes of computing cross sections we interpret these four possible combinations of responses as follows:

(1) We will assume that <u>all</u> ($\overline{C3}$, S4) events represent pass-through particles. Indeed, pass-through particles cannot count in the Cerenkov counter, C3, but will count in the detector, S4. This combination of counts could also be obtained, however, if an interaction occurred in which only slow secondaries were produced in the forward direction, with one of them counting in S4. As we have pointed out earlier, such an event is unlikely; nevertheless, the assumption made above may result in a low value for the attenuation cross section.

(2) and (3) We will assume that <u>all</u> annihilations produce a fast charged particle ($\beta \geq 0.75$) into the cone of acceptance of counter C3. Thus we interpret the events (C3, S4) and (C3, $\overline{S4}$) as representing annihilations. This allows us to estimate the partial cross section for annihilation.

(4) combination ($\overline{C3}$, $\overline{S4}$) is interpreted as an event in which an antiproton was scattered through an angle θ_c, without giving rise to fast charged secondaries into the cone of acceptance of C3. Of course, these events again may not give a true value for the scattering cross section, because this particular combination ($\overline{C3}$, $\overline{S4}$) could also result from annihilations in which no fast charged particle is produced in the forward direction and no charged particle traverses S4.

In summary we list the four types of events and their interpretations:

(1) ($\overline{C3}$, S4)--a pass-through particle,

(2) (C3, S4)--an annihilation event,

(3) (C3, $\overline{S4}$)--an annihilation event,

(4) ($\overline{C3}$, $\overline{S4}$)--a scattering event.

For measurement of the attenuation cross section for protons the above interpretation of the events was altered. Protons of 497 Mev are too slow to count in C3. Except for single-meson production, the protons cannot produce fast charged particles that count in C3. In fact, the very absence of counts in C3 when protons were attenuated lends strong support to the assumption that counts in C3 were due to annihilations when antiprotons were used.

D. Results

In Table II we have summarized the number of events of each type, together with the cutoff angle. The data were taken with the absorber in and out for both protons and antiprotons.

The formulas used for computing the total attenuation cross section σ and the statistical standard deviation $\Delta\sigma$ are respectively:

$$\sigma = \frac{1}{N} \ell n \frac{I_0}{I} \frac{I'}{I'_0} \qquad (1)$$

and

$$\Delta\sigma = \frac{1}{N}\sqrt{\frac{1}{I} - \frac{1}{I_0} + \frac{1}{I'} - \frac{1}{I'_0}} \qquad (2)$$

where I_0 and I'_0 are the numbers of incident particles with the absorber in and out respectively, I and I' are the numbers of pass-through particles with the absorber in and out respectively, and N is the thickness of the attenuator in atoms/cm^2. If we let I_{an} (and I'_{an}) be the number of annihilation events equal to (C3, S4) + (C3, $\overline{S4}$), then the partial cross section for annihilation, σ_{an}, is given by

$$\sigma_{an} = \frac{1}{N} \ln \frac{I_0 \; (I'_0 - I'_{an})}{(I_0 - I_{an}) \; I'_0} \qquad (3)$$

I_0, I, and I_{an} are also summarized in Table II. The resulting cross sections and statistical errors are given in Table III.

The errors listed in Table III represent only standard deviations due to counting statistics. It was not possible to obtain better statistical results because of the low counting rate. Some of the partial cross sections listed in Table III may not be very meaningful because of the large statistical errors.

A possible source of error, other than statistical, may be annihilation events in which no fast, charged secondary passes through C3. This effect would indicate that the partial annihilation cross sections given in Table III are too low, but would not affect the measured total-attenuation cross sections as long as there were no slow charged secondaries passing through counter S4. As it is very unlikely that a slow, charged particle can get through counter C3, the latter possible source of error should have very little effect on the total attenuation cross sections. For the copper experiment, counter C3 subtended an average solid angle of π steradians at the absorber. Crude kinematical estimates indicate that probably no more than 20% of the annihilations fail to produce a fast, charged particle into this solid angle. On the other hand, in the beryllium experiment counter C3 subtended an

Table II

Experimental results. Run I. I_0 is the number of incident particles, I is the number of unattenuated particles, and I_{an} is the number of annihilated particles.

Attenuator	Incident Particle	Cutoff Angle (deg)	S4 $\overline{C3}$	$\overline{S4}$ $\overline{C3}$	S4 C3	$\overline{S4}$ C3	I_0	I	I_{an}
8 in. Be	$\bar{p}$	18	26	32	16	17	91	26	33
none	$\bar{p}$	18	43	5	8	4	60	43	12
8 in. Be	p^+	18	518	392	1	3	914	519	-
none	p^+	18	619	76	2	4	701	621	-
3 in. Cu	$\bar{p}$	12.7	44	40	16	58	158	44	74
none	$\bar{p}$	12.7	51	6	4	5	66	51	9
3 in. Cu	p^+	12.7	447	448	-	-	895	447	-
none	p^+	12.7	211	45	-	-	256	211	-

Table III

Cross-Section results. Run I. The quantity σ is the measured attenuation cross section; σ_{an} is the partial cross section for annihilation. The errors shown are standard deviations due to counting statistics.

Attenuator	Incident Particle	Cutoff angle (deg)	σ (10^{-24}cm^2)	σ_{an} (10^{-24}cm^2)	$\frac{\sigma_{\bar{p}}}{\sigma_{p^+}}$
8 in. Be	$\bar{p}$	18	0.365±0.059	0.17±0.06	
8 in. Be	p^+	18	0.178±0.013		2.05 ± 0.36
3 in. Cu	$\bar{p}$	12.7	1.58 ±0.22	1.05±0.22	
3 in. Cu	p^+	12.7	0.780±0.069		2.02 ± 0.33

average solid angle of only $\pi/2$ steradians. In this case counter C3 may have failed to detect about 30% of the annhilation events. Therefore, the values quoted for the cross sections for annihilation represent lower limits.

E. Discussion

For both copper and beryllium, the measured cross sections for antiprotons are twice those for protons, within the statistical error of ± 15%. For copper with $\theta_c = 12.7^o$, $\sigma_{\bar{p}} = 1.58 \pm 0.22 \times 10^{-24}$ cm^2. $\sigma_p = 0.78 \pm 0.069 \times 10^{-24}$ cm^2. For beryllium with $\theta_c = 18^o$, $\sigma_{\bar{p}} = 0.365 \pm 0.059 \times 10^{-24}$ cm^2, $\sigma_p = 0.178 \pm 0.013 \times 10^{-24}$ cm^2. The attenuation cross section for beryllium (365 ± 59 mb) can be compared to a recent measurement of the total $\bar{p}$ – Be. cross section, 484 ± 60 mb,[4] determined in a good-geometry experiment. These results seem to indicate a very small elastic cross section compared to the inelastic. The annihilation cross section we obtained is 170 ± 60 mb, so there may be a considerable number of inelastic events of the nonannihilation type, although, as mentioned earlier, this annihilation cross section may be somewhat below the true value. The cross section we obtained for protons on copper is about 14% greater than that obtained by Chen, Leavitt, and Shapiro[18] at Brookhaven (0.68×10^{-24}cm^2) with a similar geometry at a somewhat higher energy (860 Mev). Our beryllium cross section for protons is almost 37% greater than that obtained at Brookhaven (0.130×10^{-24}cm^2). This apparent discrepancy could be due to the differences in energy and is geometry between the two experiments.

The results of this experiment show two features of particular interest:

a) The attenuation cross sections of antiprotons in beryllium and copper are approximately twice those of protons.

b) The most probable inelastic event for antiprotons in beryllium and copper is annihilation with a nucleon.

II. RUN II: ANTIPROTON INTERACTIONS WITH NUCLEONS AND COMPLEX NUCLEI

A. Introduction

The purpose of the first part of this experiment was to measure both the interaction and the annihilation cross sections for antiprotons on protons and neutrons. The method employed was that of measuring the cross sections of antiprotons on water, heavy water, and liquid oxygen. The D_2O and H_2O results were then subtracted, giving information about the $\bar{p}n$ interaction. Similarly, subtracting the O_2 results from those for H_2O gave information on the $\bar{p}p$ interaction.

To obtain statistically significant cross sections for the antiproton-nucleon interactions in a subtraction experiment such as this, we must measure the cross sections in D_2O, H_2O, and O_2 to a fairly high degree of accuracy. Even with the greatly increased antiproton beam intensity obtained in this run (nominally, 300 antiprotons per hr), this required a large amount of Bevatron time. However, this disadvantage of the subtraction experiment was largely compensated for by the additional information that could be obtained; namely, the total annihilation cross sections.

Emulsion experiments[7] have shown that the antiproton-nucleon annihilation process proceeds primarily through pion production. This affords us a convenient method of detecting antiproton annihilations. In nearly all annihilations some charged mesons are produced that are relativistic and will thus emit Cerenkov light in passing through H_2O, D_2O, or O_2. Also some of the γ-rays from neutral mesons produced in the annihilations will be converted in the attenuator material, resulting in relativistic electrons that emit Cerenkov light. The procedure used in detecting annihilation events was thus simply to look at this Cerenkov light in the attenuator itself. The target was a light-tight container filled with D_2O, H_2O, and O_2 in turn, viewed from the top by a layer of nine photomultiplier tubes. The threshold velocities

for charged particles producing Cerenkov light in H_2O (index of refraction n = 1.33), D_2O (n = 1.33), and O_2 (n = 1.22) are β = 0.75, 0.75, and 0.82, respectively. Hence the antiprotons themselves (β = 0.68) will not produce Cerenkov light in these substances, while mesons resulting from annihilation will. We have, therefore, a 4π geometry detector of annihilation events. This Cerenkov counter C^{**} is shown in Fig. 4.

In order to measure the cross sections for antiprotons on copper, silver, and lead, we altered the target-Cerenkov counter slightly. A container of similar size and shape was constructed, but included in the bottom were slots in which were placed the target materials. This container is shown schematically in Fig. 5. In this case the counter, labelled C^*, was filled with methyl alcohol (CH_3OH). This material was chosen as the Cerenkov radiator because of its low density (ρ = 0.80 gm/cm^3) and its index of refraction of 1.33 (velocity threshold for charged particles of β = 0.75).

As in Run I, the pass-through antiprotons were detected by a scintillation counter located some distance behind the target, C^{**}(or C^*). This counter detected all charged particles passing through it. These charged particles were (a) "pass-through" antiprotons (see Section I-A for the definition of a pass-through antiproton), and (b) charged secondaries resulting from the annihilation of an antiproton with a nucleon. However, events of type (b) would be accompanied by a count in the target counter, C^{**}, and hence no confusion should arise as to which counts in the scintillation counter represented pass-through antiprotons. During the actual experiment, two such pass-through scintillation counters were used simultaneously. These were S2 and S3, with cut-off angles of 20.5° and 14.3°, respectively.

Again the antiproton cross sections were compared with those for protons by an experiment in which the currents in the magnetic selecting channel were reversed. It was necessary to change the position of the target in the Bevatron slightly and to adjust the currents in the first part of the magnetic channel to allow the protons to pass

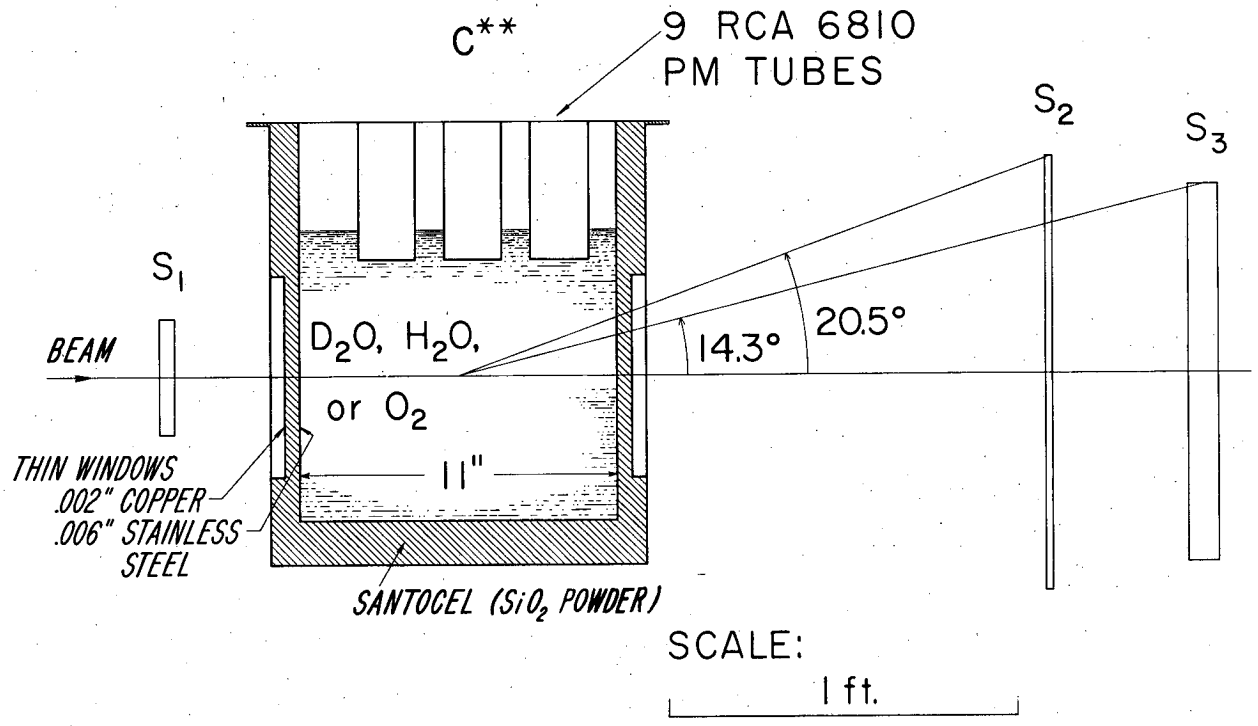


Fig. 4. Schematic diagram of geometry for antiproton-nucleon measurements, Run II.

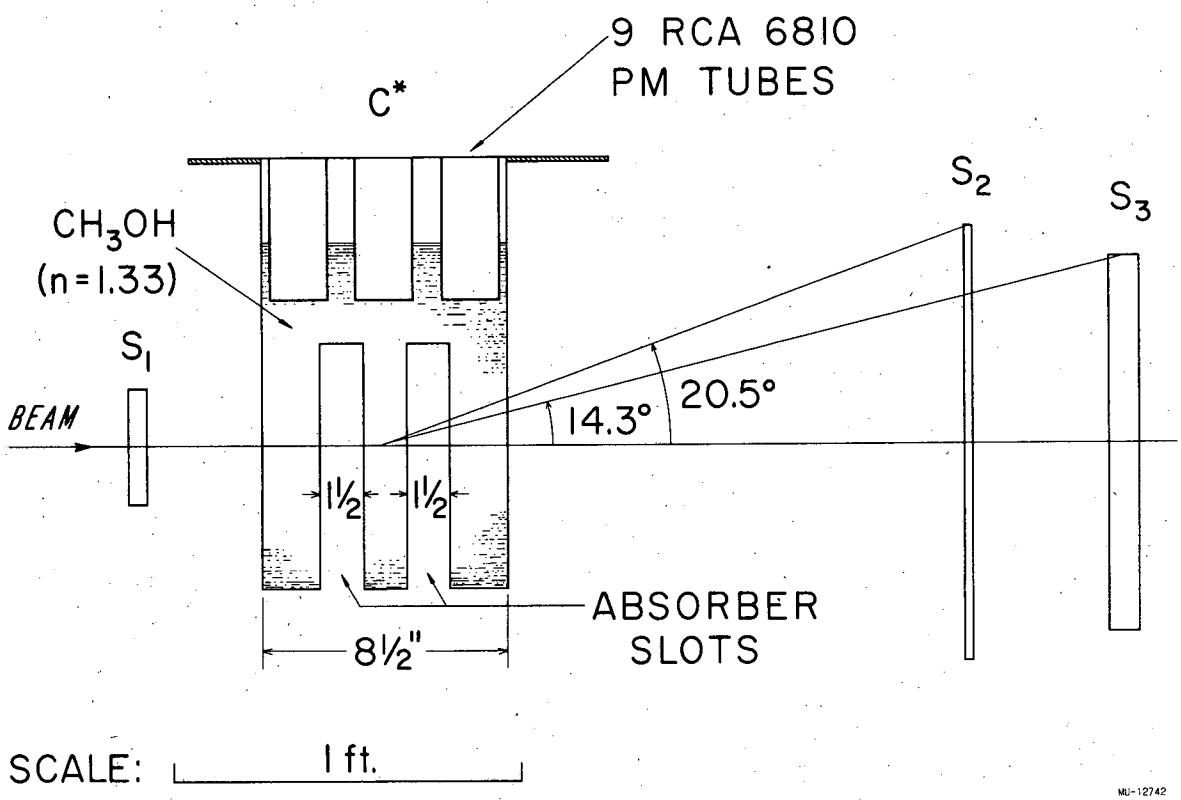


Fig. 5. Schematic diagram of geometry for measurements of interaction cross sections of antiprotons on complex-nuclei, Run II.

through the fringing field of the Bevatron into the orbit defined by the magnets and counters. For these runs the Bevatron internal beam was accelerated to 1.1 Bev. There was no meson contamination of this 1.175-Bev/c external proton beam, because mesons of this momentum could not be produced by 1.1-Bev protons.

B. The Antiproton Beam

The intensity of the antiproton beam used in Run I was approximately one antiproton every 15 min. In order to perform this subtraction experiment, it was imperative that this intensity be increased many fold. This was accomplished by revising the mass spectrograph used in Run I so as to accept particles emitted into a larger solid angle at the Bevatron target, and also to accept a momentum interval of ± 4% instead of only ±1% as before. This new system is described below; the antiproton beam intensity was increased by a factor of about 80.

The magnetic channel used to select the antiprotons in Run II is shown schematically in Fig. 6. The antiprotons produced in the 6-in.-long carbon target in the Bevatron are bent outwards by the fringing field of the Bevatron. A small magnet (D) was placed as close as possible to the structure of the Bevatron in order to guide the negatively charged beam into the remaining segments of the magnetic channel. The current in this magnet was then varied until the intensity of the negatively charged particle beam was a maximum. Upon emerging from the magnet D, the 1.2-Bev/c-antiprotons entered a magnetic-quadrupole focusing lens, Q1, with an 8-in.-diameter aperture, which focused the antiprotons at the center of a second, smaller, 4-in.-focusing quadrupole, L. Between these two quadrupoles a bending magnet, M1, deflected the antiprotons by 14°. The lens, L, served as a field lens to focus particles leaving Q1 onto the entrance aperture of the last lens, Q2. At the exit end of L was placed a counter F1 (to be described later) in which the antiprotons were reduced

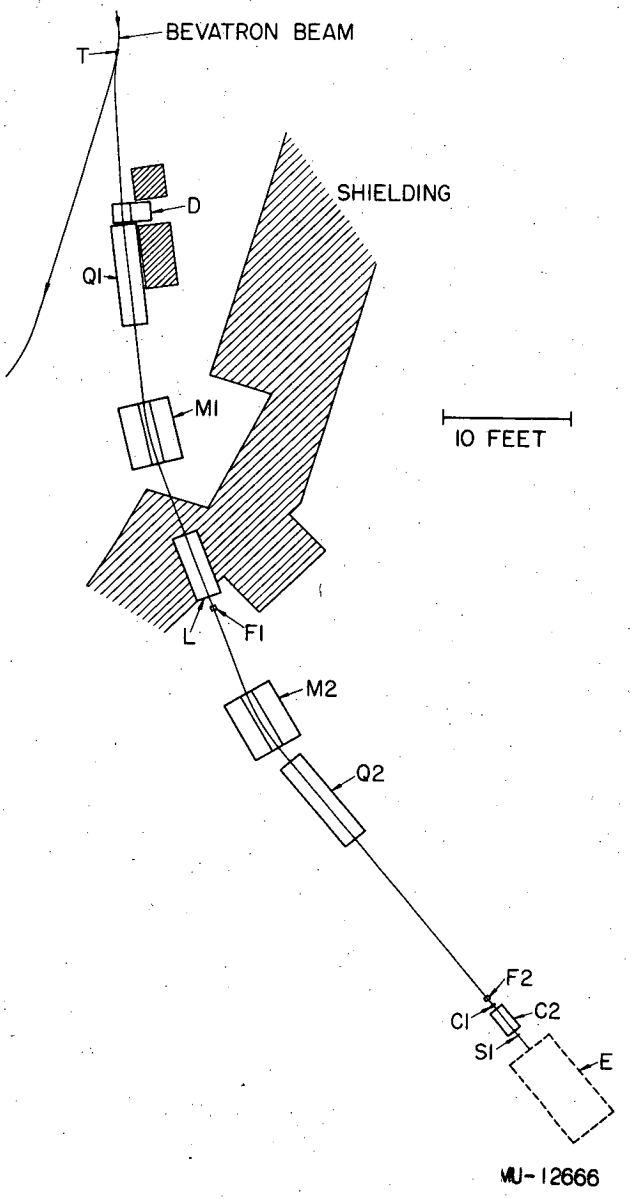


Fig. 6. Schematic diagram of antiproton-beam magnetic channel, Run II.

in momentum to 1.175 Bev/c because of ionization-energy losses. The second half of the magnetic channel was, therefore, tuned to this slightly lower momentum and consisted of a further bending of 18.8° in M2. The 1.175 Bev/c antiprotons were then focused upon F2 by another 8-in. quadrupole lens, Q2.

The momentum of the antiproton beam at F2 is 1.175 Bev/c with a spread at half maximum of ±3%. This corresponds to an energy of 565 ± 35 Mev. The horizontal-and vertical-intensity distributions of the beam at F2 are shown in Fig. 7. These graphs were obtained by measuring the charged-particle coincidence counting rate between a scintillation counter placed at F1 and a small explorer counter near F2, as a function of the horizontal and vertical positions perpendicular to the beam at F2. The horizontal width of the beam at F2 was considerably less than that at F1, because the "chromatic aberration" of the latter half of the magnet system was adjusted to compensate for that of the first half. Ionization energy loss in F2, C1, C2, and S1 reduced the mean energy of the beam to 497 Mev upon leaving S1. The diameter of the beam at this point, defined by counter S1, was 4 in. The beam leaving S1 had a root-mean-square angular divergence of ± 3° due mainly to multiple Coulomb scattering in F2, C1, and C2.

C. Experimental

1. Attenuators

As explained earlier, H_2O, D_2O, and liquid oxygen were chosen for the subtraction experiments. The thicknesses (in atoms/cm^2) were nearly the same because the same container, C**, was used for all three. This thickness was chosen to give an attenuation of approximately one-third for antiprotons, based on an assumed cross section of twice geometrical. Table IV gives some of the pertinent properties of these liquids, including the thicknesses in atoms/cm^2 in the target container, C**. Some of the factors included in the choice of these substances were density, index of refraction, transparency, amount of hydrogen contained, availability, and the ease with which they could be contained.

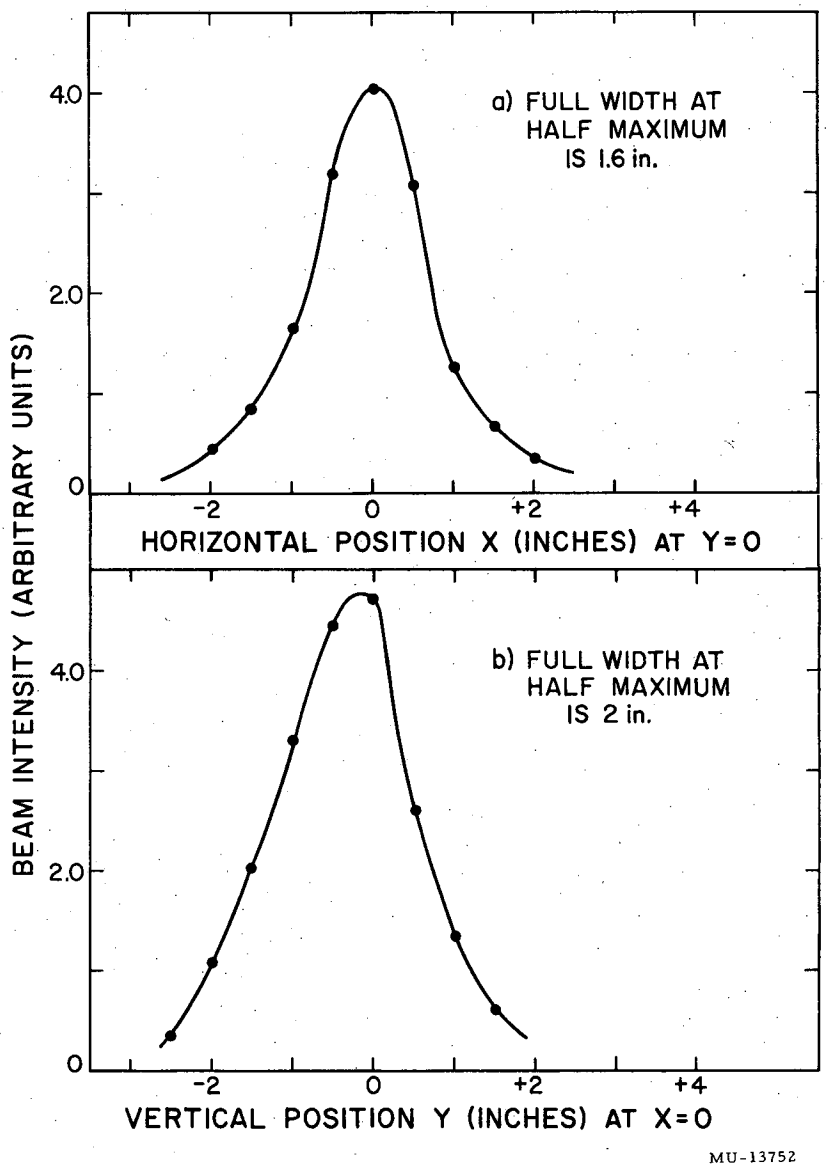


Fig. 7. (a) Horizontal beam-intensity distribution at F2.
(b) Vertical beam-intensity distribution at F2.

The elements in the complex-nuclei experiment were copper (a repeat of the measurements of Run I by a slightly different method), silver, and lead. A thickness of 3 in. was chosen for the copper absorber; the silver and lead were 2-in.-thick. These thicknesses were as large as possible consistent with a negligible amount of loss due to the multiple Coulomb scattering. This is discussed further in sections II-C2 and II-F1.

Table IV

Characteristics of Attenuator Materials: Run II

Material	Thickness ($Atoms/cm^2$)	Density (gm/cm^3)	Index of Refraction	Av. Energy of Beam at Center (Mev)
D_2O	0.910×10^{24}	1.105	1.33	457
H_2O	0.915×10^{24}	1.0	1.33	457
O_2	1.170×10^{24}	1.142	1.22	457
Cu	0.644×10^{24}	8.89	-	411
Ag	0.296×10^{24}	10.5	-	431
Pb	0.1678×10^{24}	11.34	-	436

2. Geometry

The half-angle subtended by the pass-through counter at the center of the absorber is conventionally called the cut-off angle, θ_c. The divergence of the incident beam and the thickness of the attenuators introduces an uncertainty in the real cut-off angle, especially in the experiments with the heavy elements. The smallest cut-off angle was chosen larger than the angle of the first diffraction minimum for protons on oxygen. Because of the divergence of the antiproton beam, it was necessary to make the smallest cut-off angle slightly larger than dictated by this criterion. The angle at this first minimum is given by $\sim 0.61\ \lambda/R$,

where λ is the wave length of the incident antiproton, and R is the radius of interaction of the target nucleus as seen by the incident particle (a lower limit for R is obtained from $\sqrt{\sigma_{\text{interact.}}/\pi}$). Because antiprotons have larger interaction cross sections than protons, R is larger and λ/R smaller for antiprotons. Thus both pass-through counters intercepted nearly all antiprotons that had suffered only diffraction scattering and multiple Coulomb scattering. The two cut-off angles were 14.3° and 20.5°; these remained constant throughout the experiment.

As mentioned above with regard to the heavier elements, multiple Coulomb scattering became important and limited the thickness of usable attenuators compatible with these cut-off angles.

A schematic drawing of the experimental arrangement is shown in Fig. 4 for the $\bar{p}$-nucleon experiments and in Fig. 5 for the $\bar{p}$-complex-nuclei experiments.

3. Counters

Table V lists the characteristics of the components of the apparatus used in Run II. Fig. 6 shows the positions of the counters used in separating the antiprotons from the large pion background. F1 and F2 are velocity-selecting Cerenkov counters described by Fitch.[9] These counters, which consist of liquid-styrene radiators (index of refraction = 1.543) viewed by one RCA-6810 photomultiplier tube, detect charged particles in the velocity range $0.65 \leq \beta < 0.86$. Particles with a slower velocity do not emit Cerenkov light in styrene, and the Cerenkov light from particles faster than $\beta = 0.86$ is totally internally reflected and, hence, not detected by the photomultiplier tube. About 10% of the particles with a velocity greater than $\beta = 0.86$ suffer an interaction in the radiator, the secondaries from which give rise to Cerenkov light that reaches the photomultiplier tube. F1 and F2 hence have a rejection efficiency of only about 90%. Counters C1 and C2 are also Cerenkov counters. C1 consists of fluorochemical radiator ($C_8F_{16}O$, designated 0-75 by Minnesota Mining and Manufactorying Co.) with an index of

refraction of 1.276, which counts only charged particles with $\beta > 0.78$ and hence will not detect the antiprotons but will detect the pi mesons. C2 is a special counter[10] (the same counter as C2 in Run I, but with a lucite instead of a quartz radiator) that detects charged particles in the very narrow velocity range $0.74 < \beta < 0.77$, with a rejection efficiency for faster particles of 97%. Finally, S1 is an ordinary scintillation counter 4 in. in diam which detects all charged particles passing through it. This counter defines the size and divergence of the antiproton beam incident upon the target. Thus counters F1, F2, S1, and C2 are placed in coincidence with each other and in anticoincidence with C1 to detect an antiproton. The actual electronic method of selecting the antiprotons is described in the next section.

Counter C^{**} has been discussed briefly in Section II-A and consists of a rectangular stainless steel container 10.75-in. long. When it was filled with D_2O or H_2O, the liquid level was about 0.5 in. above the faces of the nine photomultiplier tubes that were suspended from the top cover. With liquid oxygen, the liquid level had to be kept slightly below the tube faces, otherwise the tubes would not respond properly. In order to collect as much of the Cerenkov light as possible, the sides and bottom of C^{**} were lined with shiny 1-mil aluminum foil. Counter C^{*} is similar to C^{**} but has slots of dimensions shown in Fig. 5 in the bottom for insertion of the copper, silver, or lead attenuators and contains methyl alcohol as the Cerenkov radiator.

The remaining two counters, S2 and S3, are plastic scintillation counters. Counter S2 was 0.25-in. thick by 14.75 in. diam and is viewed by eight RCA 6655 photomultipliers symmetrically placed around the periphery. The signals from the eight tubes were added together and then suitably amplified. S3 is 1 in. thick and 13 in. in diam and is viewed from the side through a long Lucite light pipe by a single RCA-6810 photomultiplier tube.

Table V

Characteristics of components of the apparatus: Run II

T	Bevatron target.
F1	Cerenkov counter of styrene ($C_6H_5CH{:}CH_2$) with 2.5% ethyl bromide (C_2H_5Br) ; $\mu_D = 1.54$; $\rho = 0.91$ g cm^{-3}. Diameter 3.88 in. by 2.31 in. thick.
F2	Same as F1 except diameter 2.5 in.
C1	Cerenkov counter of Fluorochemical 0-75, ($C_8F_{16}O$); $\mu_D = 1.276$; $\rho = 1.76$ g cm^{-3}; 4 in. square by 1.5 in. thick.
C2	Cerenkov counter of lucite (polymethyl methacrylate); $\mu_D = 1.50$; $\rho = 1.18$ g cm^{-3}. Diameter 2.37 in. by 4.25 in. thick.
S1	Plastic scintillator counter 4.0 in. diameter by 0.62 in. thick.
E	Area occupied by apparatus and counters for the various experiments.
D	Deflecting magnet 18 in. long. Aperture 12 in. wide by 5 in. high. 3.2° bending.
Q1, Q2	Quadrupole focusing magnets of 8-in. aperture.
M1, M2	Deflecting magnets 60 in. long. Aperture 12 in. wide by 7 in. high. 14° bending and 18.8° bending respectively.
L	Quadrupole focusing magnet of 4 in. aperture.
C**	Attenuator and Cerenkov counter filled with D_2O, H_2O, or O_2.
C*	Slotted Cerenkov counter of methyl alcohol (CH_3OH).
S2	Plastic scintillator counter 14.75 in. diameter by 0.25 in. thick.
S3	Plastic scintillator counter 13 in. diameter by 1.0 in. thick.

4. Electronics and Photography

Figure 8 shows a block diagram of the electronics employed in this experiment. Counters F1, F2, and S1 were placed in coincidence with each other and in anticoincidence with C1 by means of a fast coincidence circuit which has a time resolution of about 4×10^{-9} sec. Counter C2, the velocity-selecting counter, consists of 3 photomultipliers looking at the same lucite Cerenkov radiator.[10] It was required that at least two out of the three tubes count in coincidence in a special coincidence circuit. The outputs of these two coincidence circuits were fed to a third coincidence circuit (AB) with a time resolution of about 2×10^{-8} sec. The resulting coincidences represented what might be called "electronically-defined" antiprotons.

However, in addition to the output pulses from antiprotons which registered a coincidence in AB, some output pulses from AB were found to be caused by accidental coincidences due to mesons. In order to recognize these accidentals, it was necessary to photograph the pulses from the various counters. The pulses from counters F1, F2, and C1 were delayed and then displayed on the top trace (No. 1) of a 4-beam oscilloscope tube, pulses from counters S1, and C^{**} on trace No. 2, and pulses from S2 and S3 were recorded on trace No. 3. Trace 4 was not used in this part of the experiment. The output from the AB coincidence circuit was used to trigger the oscilloscope, which was being continuously photographed on linagraph-pan 35-mm film.

When positive proton cross sections were measured, it was not necessary to look at pulses in the C^{**} counter because annihilations do not take place. Furthermore, there was no meson contamination of the proton beam as explained in Section II-A. This lack of contamination allowed us to measure the cross sections electronically by use of two additional coincidence circuits, YES and NO, shown in Fig. 8. Counter S2 was placed in coincidence with the output from AB by means of the YES circuit, and S3 was put in coincidence with AB by means of the NO circuit. The outputs from the YES and NO circuits were fed to scalers

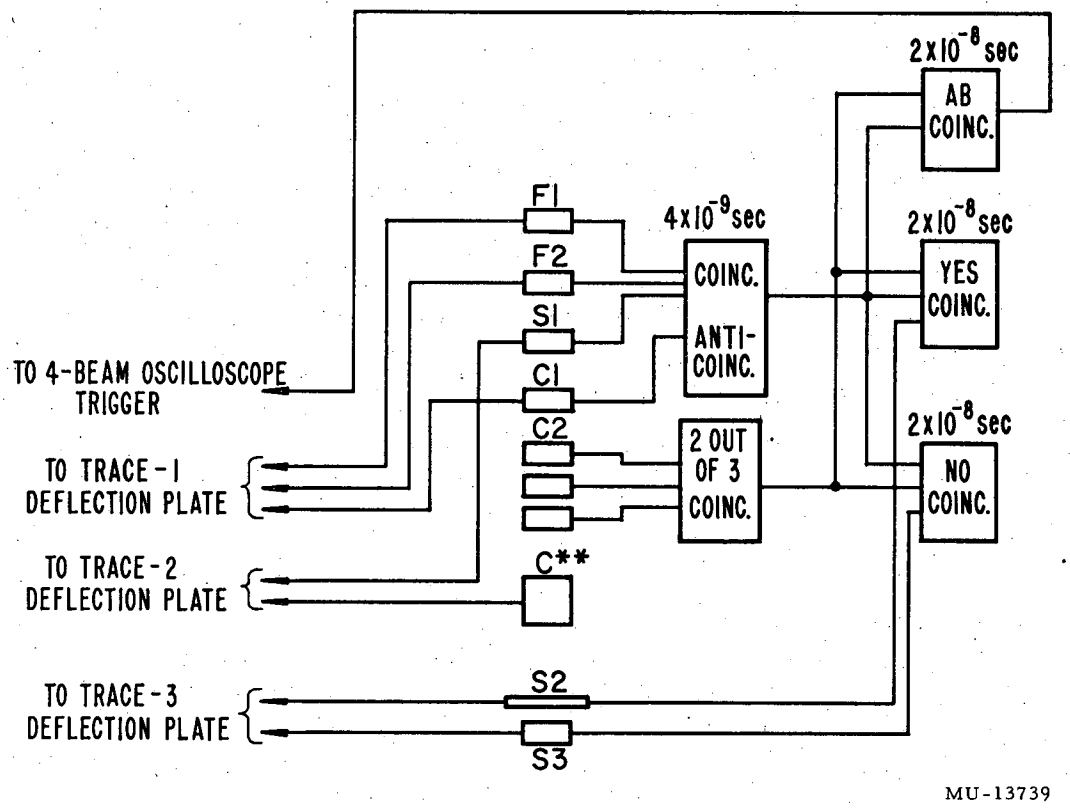


Fig. 8. Block diagram of electronics, Run II.

that registered the number of incident protons that also counted in S2 and S3, respectively. A check on this electronic measurement of the cross sections for protons was made by photographing proton events in the same manner as the antiproton events.

5. Procedure

The Bevatron internal proton beam was accelerated to full energy, 5.8 to 6.3 Bev. The internal beam intensity used was approximately 2 to 3 x 10^{10} protons per pulse. The number of accidental coincidences were reduced by spilling the internal circulating beam onto the carbon target over as long a time as was possible--usually from 80 to 120 msec. This was accomplished by steering the full energy beam repeatedly through a thin aluminum foil near the outer radius of the Bevatron orbit. The degraded beam then became phase-unstable and spiralled into the carbon target over a period of time determined by the rate at which the initial beam was steered into the foil. The resultant proton beam striking the carbon target had an energy range from 5.8 to 6.3 Bev.

The internal proton beam striking the carbon target was monitored by means of an auxilliary system of two counters in coincidence aimed roughly at the target and about fifteen feet away from it. We thus had a continuous check on the uniformity of the internal beam which was being spilled onto the carbon target. The electronic apparatus was gated on at the beginning of the beam spill-out and gated off at the end, about 100 msec later.

In order to obtain antiproton-nucleon cross sections with a statistical accuracy of about ± 10%, it was necessary to take the data for D_2O, H_2O, and O_2 until nearly 10,000 antiprotons were incident upon each of these materials. The three absorber materials were cycled through several times. In addition, because some of the annihilations in C^{**} may result in small C^{**} pulses and hence in a slight inefficiency in detecting annihilations, the data were taken at several gains for the counter C^{**}. In particular, the O_2 data were taken at an input voltage to the photomultipliers of 2050 v, the H_2O data at both 1900 and 2000 v, and the D_2O data at

1900, 2000, and 2100 v. The data with copper, silver, and lead in the slots of C^* were taken at voltages of 2000 and 2200 v. In addition, data were taken at 2000 and 2200 v with no attenuator in the slots of C^*.

Finally, with the delays in the counters unchanged, the magnetic channel was tuned for a 20% lower mass than that of the antiproton by reducing the currents in the magnets by 20%. The events that now resulted in AB coincidences (see Figs. 9 and 10) were photographed. None of these accidental events could be interpreted as antiprotons upon examination of the photographed oscilloscope sweeps. Hence, we believe that, for the accuracies of this experiment, any contamination of the events accepted as antiprotons is negligible.

D. Reduction of Data

1. Film Reading

Figures 9 and 10 show examples of 6 of the many types of events recorded on the film. The top trace in each event shows from left to right pulses from F1, F2, and C1. The second trace shows pulses from S1 and C^{**}, and the third trace shows the pulses from S2, and S3, respectively from left to right. The individual events are described in the figure legends. The occurrence of an antiproton incident on the attenuator C^{**} (or C^*) is indicated by the presence of F1, F2 and S1 pulses, and the absence of the C1 pulse.

In reading the film, the data recorded from each event were the pulse heights (in mm, as measured on the screen of the viewer,) of the pulses from counters C1 and C^{**} and the existence or nonexistence of pulses from S2 and S3. Only those events were accepted that had a pulse for F1, F2, and S1, although all events were recorded. In addition, it was required that no spurious pulses (mainly due to extraneous mesons passing through the system) occur within a specified distance of any of the "normal" pulses. Thus an event of the type shown in Fig. 10b would be rejected. These strict criteria were adopted to avoid bias in the reading of the film.

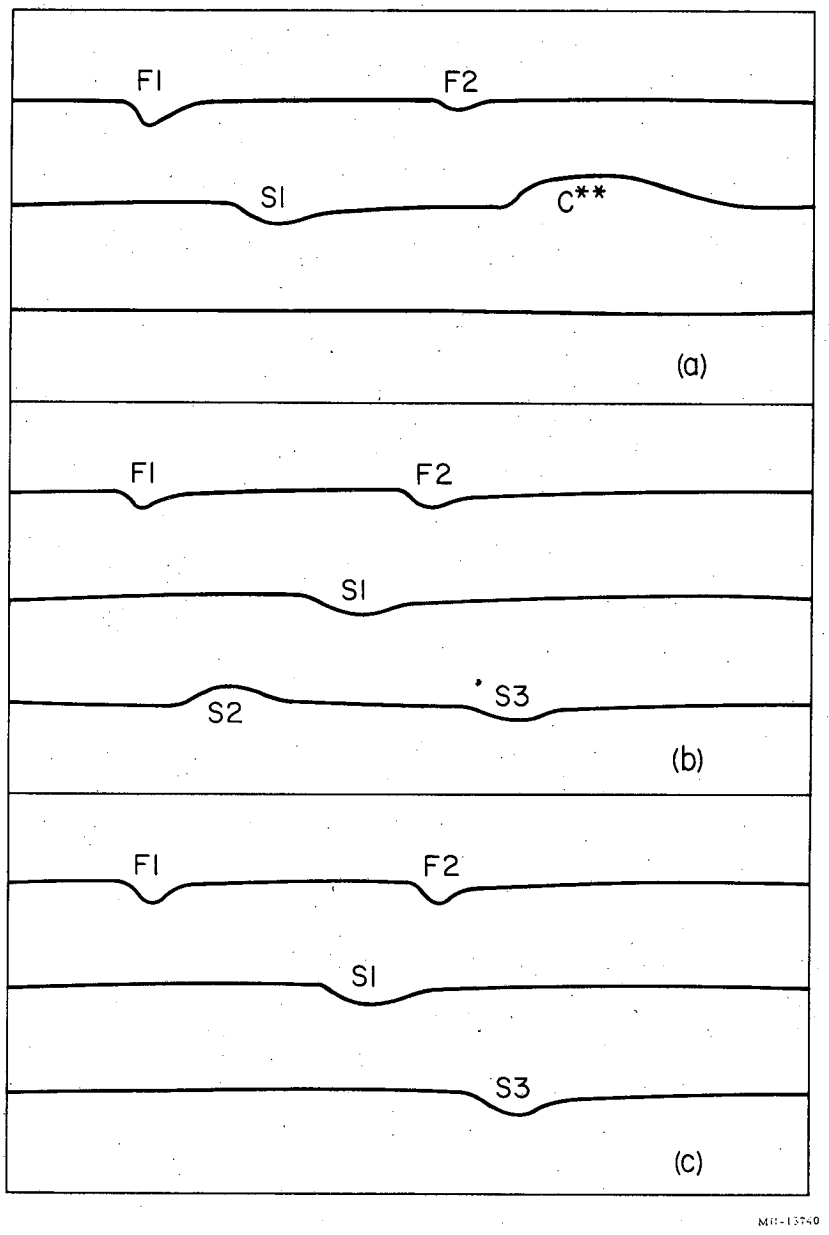


Fig. 9. Examples of oscilloscope traces. In each example, the top sweep shows pulses from left to right of F1. F2, and C1. The second trace shows pulses from S1 and C**, and the third sweep S2 and S3, respectively, from left to right. Example (a) shows an antiproton that annihilates in C** as indicated by the large C** pulse. The second (b) and third (c) events show antiprotons that do not annihilate, the first simply passing through both S2 and S3, and the second being scattered out of S3 (14.3^{o}) but not scattered out of S2 (20.5^{o}).

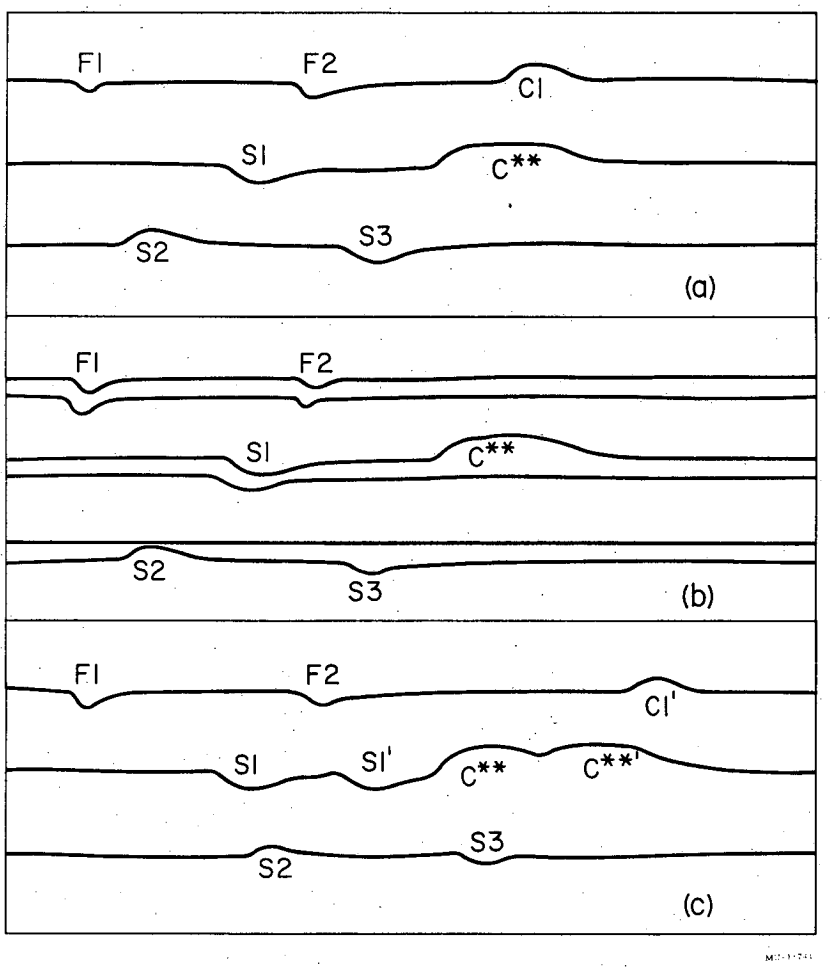


Fig. 10. Examples of oscilloscope traces. In each example the top sweep shows pulses from left to right of F1, F2, and C1. The second trace shows pulses from S1 and C**, and the third sweep, S2 and S3, respectively, from left to right. Example (a) is a meson accidental as identified by the large pluse in C1. Event (b) shows two antiprotons occurring during the same Bevatron pulse. Event (c) shows an antiproton incident upon the system of counters, with a meson following closely behind.

2. IBM-650 Analysis

The data recorded by the film readers was punched on standard 80-column IBM cards. All pulse heights greater than 9 mm were punched as 9 mm on these cards. The cards were then processed by the IBM-650 magnetic-drum data-processing machine. The IBM-650 was programmed to discard all events not acceptable under the criteria mentioned above.

In order to make a pulse-height analysis of the counts in $C_{,}^{**}$ each acceptable event was classified according to its pulse height in C^{**} and according to whether or not the particles counted in S2 and S3. The values of the pulse height of C^{**} range from zero through nine--10 values. There are four possible permutations of the two pass-through counters S2 and S3: S2S3, S2$\overline{S3}$, $\overline{S2}$S3, and $\overline{S2}\overline{S3}$, where S2 means S2 counted, and $\overline{S2}$ means that S2 did not register a count. Hence, each acceptable event was placed by the 650 calculator into one of these 40 "boxes". It is then easy to plot the pulse-height distribution of $C_{,}^{**}$ for example, for all events that either do or do not count in S3.

3. Notation

An antiproton incident on the attenuator C^{**} must always count in S1. The total number of incident particles (equal to the number of counts in S1) will be called I_0. For the purpose of computing cross sections, the following notation will be used:

(a) I_0 – the number of incident particles on the attenuator or the total number of acceptable events.

(b) I_{an} – the number of annihilation events

(c) $I(20^\circ)$ – the number of "pass-through" particles as defined in Section IV-A, with a cut-off angle $\theta_c = 20.5^\circ$. This equals the number of nonannihilation events that count in S2.

(d) $I(14^\circ)$ – the number of pass-through particles with a cut-off angle $\theta_c = 14.3^\circ$. This equals the number of nonannihilation events that count in S3.

(e) $I_{an}(20^{o})$–the number of annihilation events in which a charged particle counts in S2.

(f) $I_{an}(14^{o})$–the number of annihilation events in which a charged particle counts in S3.

(g) $I_{an}(>20^{o})$–the number of annihilation events in which no charged particle counts in S2.

(h) $I_{an}(>14^{o})$–the number of annihilation events in which no charged particle counts in S3.

We have the following obvious relations:

$$I_{an} = I_{an}(20^{o}) + I_{an}(>20^{o}) = I_{an}(14^{o}) + I_{an}(>14^{o}), \quad (4)$$

$$I_{an}(20^{o}) + I(20^{o}) = \text{total number of counts in S2, and} \quad (5)$$

$$I_{an}(14^{o}) + I(14^{o}) = \text{total number of counts in S3.} \quad (6)$$

4. Interpretation of C^{**} pulses

The problem at hand is to determine from the data the quantities I_0, I_{an}, $I(14^{o})$, and $I(20^{o})$. This is not quite as simple as it might seem at first glance. The difficulty arises in interpretation of the small C^{**} pulses. There is no obvious pulse height for C^{**} for which one can say all pulses greater than this value represent annihilations and all others represent nonannihilation events. Indeed, this is not even what we expect. Emulsion data[7] have indicated that some annihilations occur in which no fast charged particle escapes the nucleus; either all fast charged particles resulting from the annihilation are absorbed by the nucleus, or the annihilation proceeds through production of only neutral pions. Both of these types of events will result in no pulse in C^{**} except for those cases when the γ's from the neutral pions convert in the attenuation, in which case we may get small pulses in C^{**}. Further, small C^{**} pulses are expected to result also from annihilations near the end of the attenuator C^{**} where the path length for the resulting fast, charged mesons may be so short that very little Cerenkov light is emitted. Thus we conclude that a few annihilations will give small pulses in C^{**} and some of the annihilation events will result in no pulse in C^{**}.

Let us approach the problem from the other direction and ask if small C^{**} pulses can be produced by antiprotons that merely pass through C^{**} suffering no nuclear interaction. This is best answered by studying the pulse-height distribution of C^{**} pulses when positive protons are incident. Figure 11 shows examples of these pulse-height distributions for protons at two different input voltages on C^{**} for C^{**} filled with D_2O. We notice that a few small pulses occur in C^{**} (The few large pulses observed are probably due to meson production.) The momentum of the proton beam was lowered to 1.059 Bev/c, well below the velocity at which protons begin to make Cerenkov light in D_2O. Approximately the same number of small C^{**} pulses are present (Fig 12), probably indicating a small amount of scintillation. Similar results were found with the other radiators used in C^{**} and C^{*}, H_2O, O_2, and methyl alcohol.

We may conclude that only some of the small pulses in C^{**} represent annihilations, and that some annihilations are included in the events with no pulse in C^{**}. However, this dilemma is not unresolvable. To determine the correct number of annihilations, we plotted the number of events with a C^{**} pulse height greater than a given value versus this pulse-height value (see Figures 13 through 16). The points of this curve represent the integral of the pulse-height histogram from the right. We have included in this plot only those C^{**} pulses that are large enough to assure that they represent annihilations. This procedure was followed for the events that counted in S2 (and separately for events that counted in S3), and also for those events that did not count in S2 (and separately those not counting in S3). The problem of the small C^{**} pulses does not arise in events that do not result in a count in the forward counters (see Figs. 14 and 16, for example), because only a small fraction of these events are nonannihilation events so that a negligible number of pulses due to scintillations are encountered. For this reason, the integral-bias curve for these events also includes those events with very small C^{**} pulses, and no difficulty is encountered in extrapolating to zero C^{**} pulse height to obtain accurately the total number of annihilations (including those with zero pulse height in C^{**}) in which no charged particle is detected in the pass-through counter, $I_{an}(>\theta_c)$.

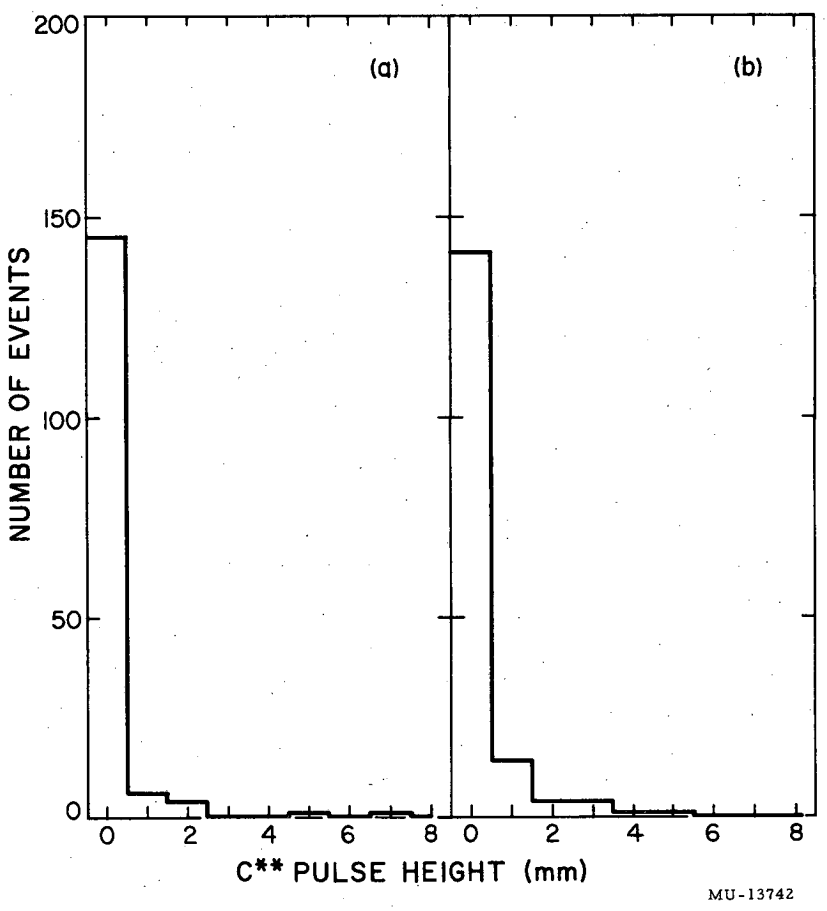


Fig. 11. Pulse-height histogram for 1.175 Bev/c protons on D_2O at C** voltages of (a) 2000 v, and (b) 2100 v.

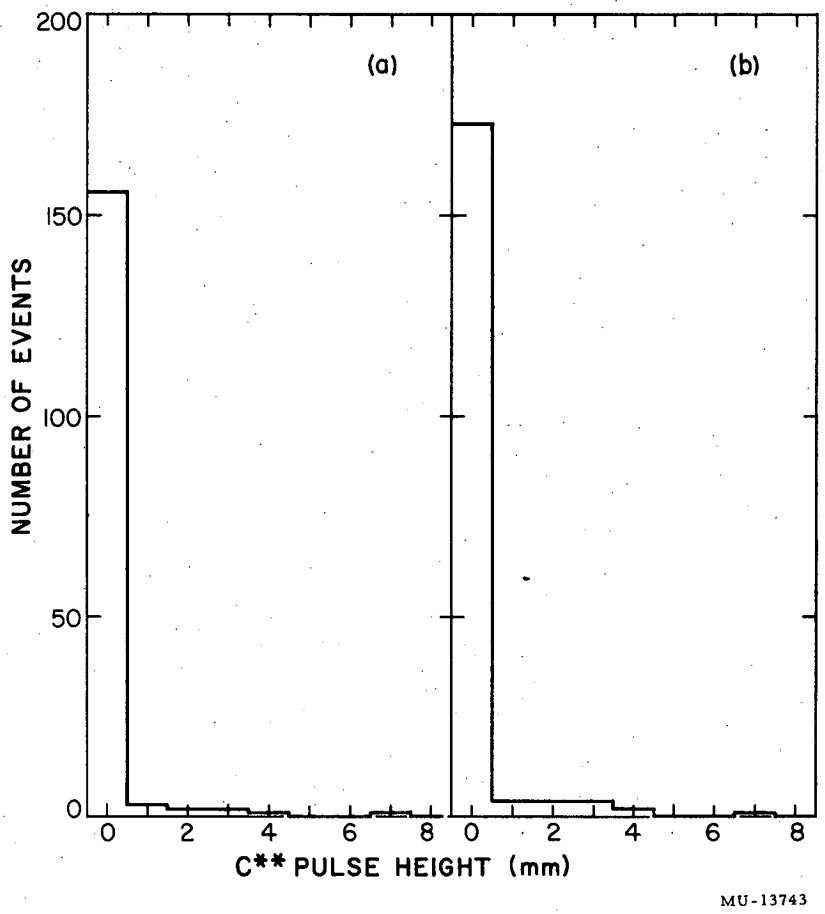


Fig. 12. Pulse-height histogram for 1.059 Bev/c protons on D_2O at C** voltages of (a) 2000v, and (b) 2100 v.

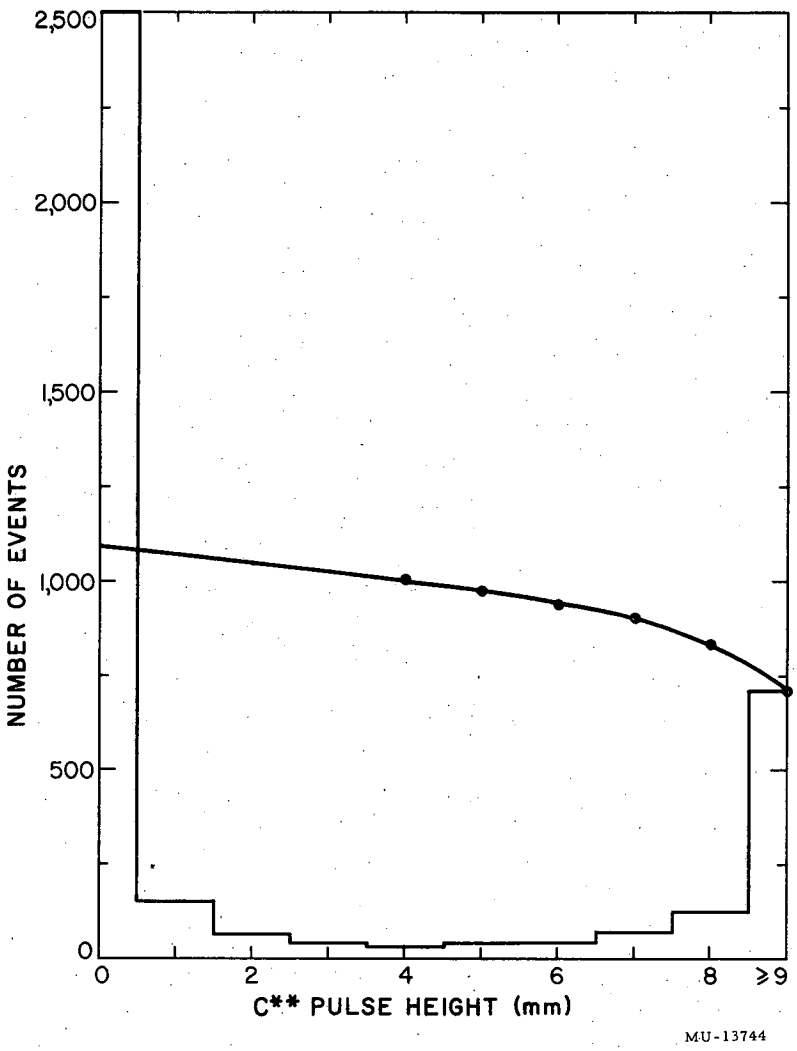


Fig. 13. Pulse-height histogram for 1.175 Bev/c antiprotons on D_2O with 2000 v on C**. Only events in which S2 counted are included. The solid curve is the integral of the histogram from the right, and only the large pulses for C** are included so as to assure that only annihilations are included.

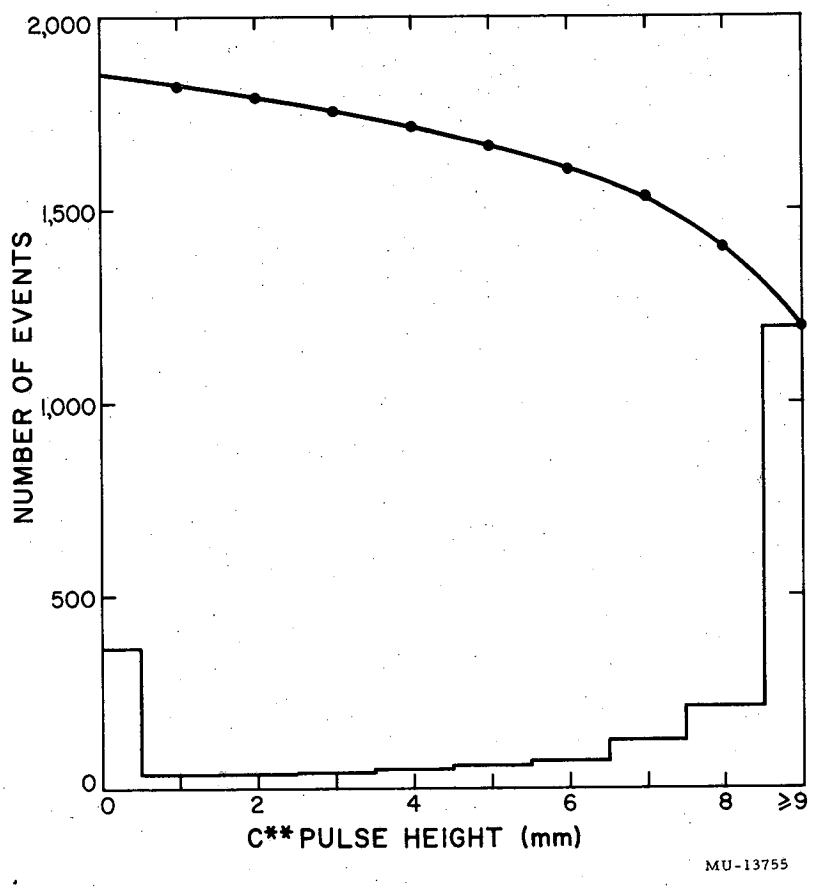


Fig. 14. Same as Fig. 13 except that only events in which S2 did not count are included.

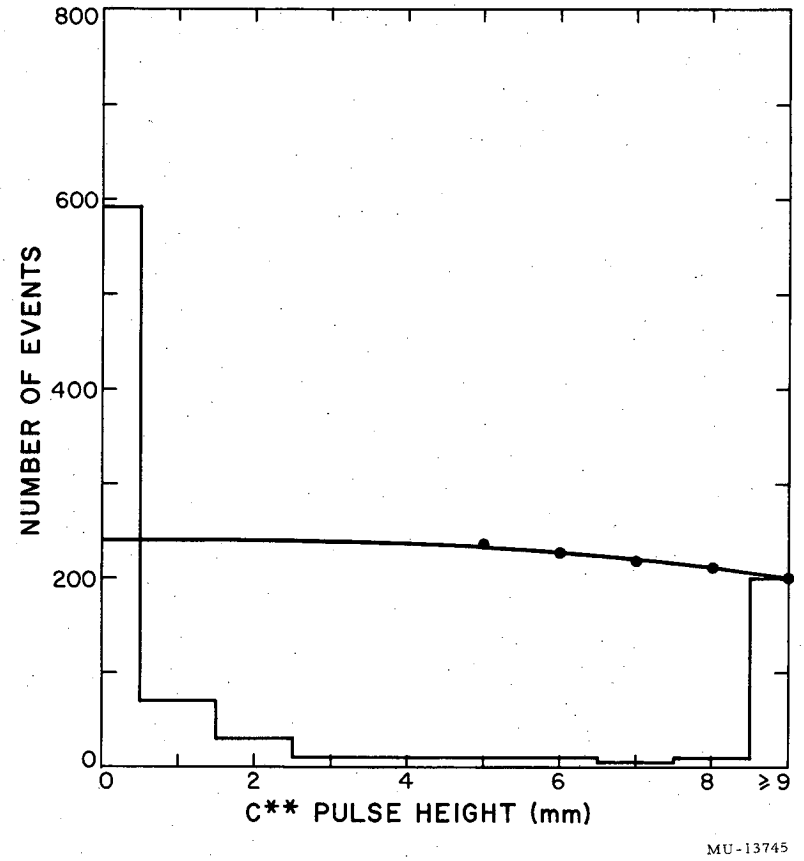


Fig. 15. Same as Fig. 13 except with 2100 v on C**.

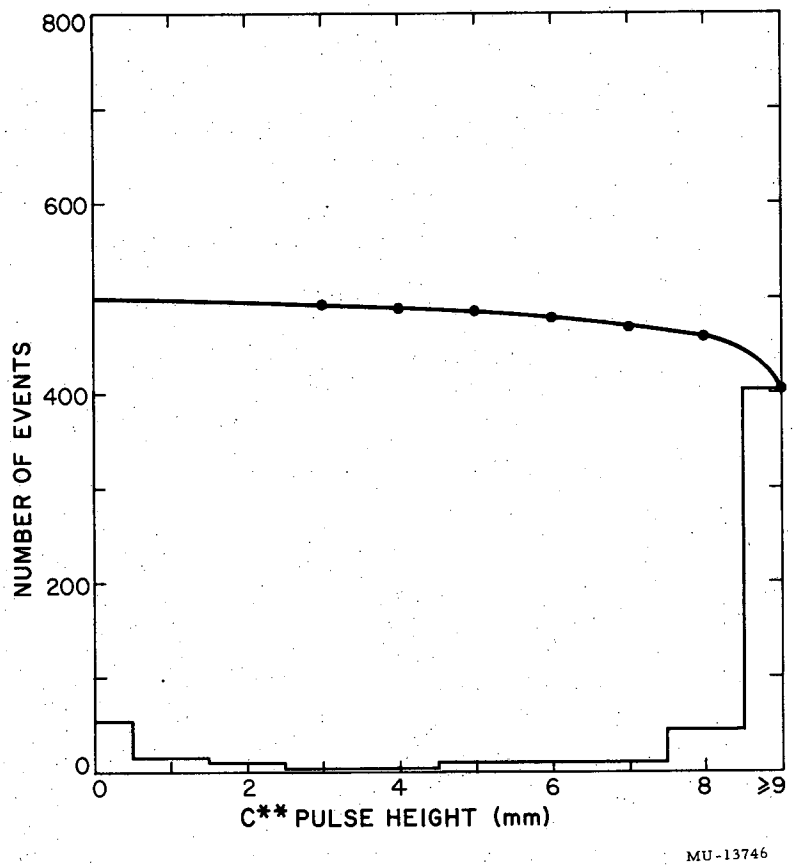


Fig. 16. Same as Fig. 15 except that only events in which S2 did not count are included.

A similar procedure was followed in treating the events in which a particle was detected in the pass-through counter. Because these events include all the pass-through particles, some small C^{**} pulses will be due to scintillations as explained above, and, hence, the points on the integral curve for small C^{**} values are not reliable and not included in the plot. To aid in extrapolating to zero C^{**} pulse height, the assumption was made that the curve shape should be similar to that for the annihilations in which no forward particle is detected. This is identical to assuming similar pulse-height distributions for C^{**} for those annihilation events in which there is no forward charged product and for those annihilations in which there is a forward charged product. It may be argued that this assumption is not strictly valid, because those annihilations taking place near the end of the attenuator C^{**} which may give rise to small pulses in C^{**} are more likely to send a charged particle through the pass-through counter because of the greater subtended solid angle. However, this effect is thought to be small enough to justify the method employed, so that the extrapolated method gives very nearly the correct total number of "forward" annihilations, $I_{an}(\theta_c)$. Examples of the histograms and extrapolations are shown in Figs. 13 through 16 for C^{**} filled with D_2O.

The total number of annihilations is obtained through application of equation 4, $I_{an} = I_{an}(\theta_c) + I_{an}(>\theta_c)$. The number of pass-through particles is obtained by means of equations 5 and 6, $I(20^\circ)$ = the number of counts in S2 minus $I_{an}(20^\circ)$, and $I(14^\circ)$ = the number of counts in S3 minus $I_{an}(14^\circ)$. It is very important to recognize that for the H_2O, D_2O, and O_2 experiment, a very large fraction of the counts in the pass-through counters actually represent pass-through antiprotons as defined earlier, and that $I_{an}(\theta_c)$ is only a small fraction of these counts. Therefore, even if a considerable error were made in the value of $I_{an}(\theta_c)$ obtained by the above extrapolation method, it would affect only very slightly the value of the total cross section, which involves only I_0 and $I(\theta_c)$. In fact, the number of annihilations that send a charged product forward into S3 is only about one-third of the

total number of annihilation events so that I_{an} is not greatly affected by an error in I_{an} (14^{o}). The same considerations hold for S2.

The data taken at the various C^{**} voltages has been treated separately, as required by the extrapolation method used. Table VI summarizes the results of these extrapolations, listing I_0, $I(14^{o})$, $I(20^{o})$, I_{an}, $I_{an}(14^{o})$, and $I_{an}(20^{o})$ for each attenuating material, D_2O, H_2O, and O, at each C^{**} voltage. Table VI also contains the extrapolation results for copper, silver, and lead.

Table VI

Experimental results, Run II. I_0 is the number of incident particles, $I(14^{o})$ and $I(20^{o})$ are the numbers of pass-through particles into the forward cone of half-angle 14.3^{o} and 20.5^{o} respectively. I_{an} is the number of annihilations and $I_{an}(14^{o})$ and $I_{an}(20^{o})$ are the numbers of annihilations in which a charged product is detected in the forward cones.

Target	C^{**} or C^{*} voltage	I_0	$I(14^{o})$	$I(20^{o})$	I_{an}	$I_{an}(14^{o})$	$I_{an}(20^{o})$
D_2O	1900	3288	1467	1522	1538	320	518
D_2O	2000	5961	2590	2684	2916	668	1090
D_2O	2100	1521	658	714	737	157	237
H_2O	1900	3539	1772	1844	1523	307	505
H_2O	2000	5377	2663	2767	2382	516	825
O_2	2050	6717	3500	3667	2760	704	1000
Cu	2000	884	298	305	520	75	140
Cu	2200	1067	330	346	660	130	192
Ag	2000	791	350	357	401	67	127
Pb	2000	939	424	444	443	97	115
Pb	2200	887	373	410	422	70	110
Methyl alcohol (slots empty)	2000	750	544	564	155	34	54
Methyl alcohol (slots empty)	2200	350	241	241	95	31	41

E. Antiproton-Nucleon Cross Sections

1. Formulas and Results

The formula for the attenuation cross sections $\sigma(\theta_c)$ for D_2O, H_2O, and O_2 at a cut-off angle θ_c is:

$$\sigma(\theta_c) = \frac{1}{N} \ell n \frac{I_0}{I(\theta_c)} \frac{I'(\theta_c)}{I'_0} = \frac{1}{N} \ell n \frac{I_0}{I(\theta_c)} - \frac{1}{N} \ell n \frac{I'_0}{I'(\theta_c)} \quad (7)$$

where I_0 is the number of incident particles, $I(\theta_c)$ is the number of pass-through particles as defined earlier, and N is the thickness of the attenuator in atoms/cm^2 (see Table IV). The primes refer to data that would have been taken with C** empty--i.e., background data. This background data was not taken because there was only a very small amount of material in the beam, other than the D_2O, H_2O, or O_2, and the error incurred in assuming $I'(\theta_c) = I_0$ is, therefore, small. In calculating the antiproton-nucleon cross sections, the D_2O, H_2O, and O_2 results are subtracted, and hence this background effect very nearly subtracts out anyway. The error introduced by this simplification is discussed further in the following section. The D_2O, H_2O, and O_2 cross sections were, therefore, calculated from the equation:

$$\sigma(\theta_c) = \frac{1}{N} \ell n \frac{I_0}{I(\theta_c)} \quad (8)$$

The formula for the standard deviation $\Delta\sigma'(\theta_c)$ due to counting statistics is:

$$\Delta\sigma'(\theta_c) = \frac{1}{N} \left(\frac{1}{I(\theta_c)} - \frac{1}{I_0} \right)^{1/2} \quad (9)$$

and the combined error $\Delta\sigma(\theta_c)$ due to counting statistics and extrapolation errors is given by

$$\Delta\sigma(\theta_c) = \frac{1}{N} \left\{ \left(\frac{1}{I(\theta_c)} - \frac{1}{I_0} \right) + \left(\frac{dI_{ns}}{I(\theta_c)} \right)^2 \right\}^{1/2} \quad (10)$$

where dI_{ns} is the nonstatistical uncertainly in $I(\theta_c)$, i.e., the estimated uncertainty in the extrapolation. The total annihilation cross section σ_{an} and its error are given by (again neglecting background effects)

$$\sigma_{an} = \frac{1}{N} \ell n \frac{I_0}{I_0 - I_{an}} \tag{11}$$

and

$$\Delta\sigma_{an} = \frac{1}{N}\left\{\left(\frac{1}{I_0 - I_{an}} - \frac{1}{I_0}\right) + \left(\frac{dI_{an_{ns}}}{I_0 - I_{an}}\right)^2\right\}^{1/2} \tag{12}$$

where $dI_{an_{ns}}$ is the estimated possible error in I_{an} due to the extrapolation.

Once the cross sections for antiprotons on D_2O, H_2O, and O_2 are determined, the measured antiproton-nucleon attenuation and annihilation cross sections $\sigma_{\bar{p}p}(\theta_c)$, $\sigma_{\bar{p}p}(an)$, $''\sigma_{\bar{p}n}''(\theta_c)$, $''\sigma_{\bar{p}n}''(an)$ are given by:

$$\sigma_{\bar{p}p}(\theta_c) = \frac{1}{2}\left[\sigma^{H_2O}(\theta_c) - \sigma^{O}(\theta_c)\right] \tag{13}$$

$$\sigma_{\bar{p}p}(an) = \frac{1}{2}\left[\sigma^{H_2O}(an) - \sigma^{O}(an)\right] \tag{14}$$

$$''\sigma_{\bar{p}n}''(\theta_c) = \frac{1}{2}\left[\sigma^{D_2O}(\theta_c) - \sigma^{H_2O}(\theta_c)\right] \tag{15}$$

$$''\sigma_{\bar{p}n}''(an) = \frac{1}{2}\left[\sigma^{D_2O}(an) - \sigma^{H_2O}(an)\right]. \tag{16}$$

The quotations are placed on $''\sigma_{\bar{p}n}''$ to indicate that no correction has yet been made for the shielding of the neutron by the proton in the deuteron. We also have for the antiproton-deuteron cross sections:

$$\sigma_{\bar{p}d}(\theta_c) = \frac{1}{2}\left[\sigma^{D_2O}(\theta_c) - \sigma^{O}(\theta_c)\right] \tag{17}$$

$$\sigma_{\overline{pd}}(an) = \frac{1}{2}[\sigma^{D_2O}(an) - \sigma^{O}(an)] \qquad (18)$$

The cross sections for antiprotons on D_2O, H_2O, and O_2 are listed in Table VII. Because the results for the different values of high voltage on C^{**} are statistically the same, these results were combined and are also given in Table VII. The resulting antiproton-proton, "antiproton-neutron", and antiproton-deuteron cross sections are given in Table VIII.

The cross sections for positive protons on D_2O, H_2O, and O_2 are included for comparison in Table VII, and the resulting pp, pn, and pd cross sections in Table VIII. Because protons do not annihilate, the uncertainty in extrapolation of C^{**} pulses does not exist, and the errors listed are standard deviations due to counting statistics only. It should be mentioned that the proton cross sections were obtained both electronically and photographically and, although the statistical errors in the latter case are large, the two methods gave consistent results. The proton cross sections were measured to provide (a) a check on the experimental method, and (b) a direct comparison of antiproton and proton cross sections under identical experimental conditions. These cross sections agree favorably with those measured elsewhere.[8] We see that the antiproton cross sections are in all cases much larger than the corresponding proton cross sections.

2. Errors

The errors on the cross sections listed in the Tables include only standard deviations due to counting statistics and the estimated errors in the extrapolations. It is pointed out here again that the uncertainty in the extrapolations introduces only a small error in the cross sections. Any error resulting from contamination of the antiproton beam is considered negligible because accidental mesons could not produce the correct arrangement of pulses required of an antiproton (see the discussion in Section C-5). Inaccuracies in interpreting

Table VII

Attenuation and annihilation cross sections for antiprotons and protons in D_2O, H_2O, and O_2. Average antiproton energy is 457 Mev. $\sigma(\theta_c)$ is the measured attenuation cross section and σ_{an} the annihilation cross section (in mb).

Target	C** voltage	$\sigma(14^\circ)$		$\sigma(20^\circ)$		σ_{an}	$\sigma(14^\circ)-\sigma(20^\circ)$
		$\bar{p}$	p^+	$\bar{p}$	p^+	$\bar{p}$	$\bar{p}$
D_2O	1900	883±21		851±21		697±18	
D_2O	2000	917±16		877±17		743±15	
D_2O	2100	882±33		837±32		733±29	
H_2O	1900	747±22		718±21		621±18	
H_2O	2000	771±16		731±16		644±15	
O_2	2050	556±10	292±2	517±10	246±2	453±9	39±3.2
D_2O	combined data for various voltages	902±11	400±2	862±11	337±2	721±11	39±4.9
H_2O		763±12	343±2	721±12	295±2	630±11	42±3.1

Table VIII

Antiproton-nucleon cross sections at 457 Mev, using $D_2O-H_2O-O_2$ subtraction (in mb).

Target	$\sigma(14^\circ)$		$\sigma(20^\circ)$		σ_{an}	$\sigma(14^\circ)-\sigma(20^\circ)$
	$\bar{p}$	p^+	$\bar{p}$	p^+	$\bar{p}$	$\bar{p}$
proton	104±8	25±1	102±8	24±1	89±7	2 ± 4
"neutron"	70±8	29±1	70±8	21±1	46 ±8	0 ± 4
$(\text{neutron})^{corr}$	108±8	32±1	108±8	23±1	74± 8	0 ± 4
deuteron	174±8	54±2	172±8	45±2	135±7	2 ± 6

"neutron": = deuteron - proton

$(\text{neutron})^{corr}$ = corrected for shielding by proton in deuteron according to Blair.[12] Errors here do not include errors involved in the correction.

the pulses on the film contribute a negligible source of error. This has been checked by a rescanning of portions of the film.

It should be mentioned that because the antiproton data at 20.5^{0} and at 14.3^{0} were taken simultaneously (particles counting in S3 also registered a count in S2), the error in the difference between the two cross sections $\sigma(14^{0})$ and $\sigma(20^{0})$ is quite small. The formula for the error in this difference is:

$$\Delta[\sigma(14^{0}) - \sigma(20^{0})] = \frac{1}{N}\left[\frac{1}{I(14^{0})} - \frac{1}{I(20^{0})}\right]^{1/2} \qquad (19)$$

The quantity $[\sigma(14^{0}) - \sigma(20^{0})]$ and its error are given in the last column in Table VII for D_2O, H_2O, and O_2, and in the last column in Table VIII for the $\bar{p}p$, $\bar{p}n$, and $\bar{p}d$ cross sections.

In order to avoid any error in N due to the bulging of the thin windows at the ends of the target C^{**} the length of C^{**} was measured when full of H_2O. The densities used in calculating N are (in g/cm^3): H_2O, $\rho=1.000$; D_2O, $\rho=1.105$; and O_2; $\rho=1.141$. The D_2O used in this experiment was analyzed chemically and found to be more than 99.5 % pure.

A small error is made in calculating the cross sections according to formula (8). No correction has been made for the attenuation of antiprotons in the material at the ends of the C^{**} container--the equivalent of about 0.5 gm/cm^2 of copper for the annihilation of $\bar{p}$. The correct formula for calculating the cross section for D_2O, H_2O, or O_2 is

$$\sigma = \frac{1}{N} \ln \frac{I_0}{I} \frac{I'}{I'_0} \qquad (1)$$

where the primes refer to data that would have been taken with C^{**} empty (see the discussion in Section II-E1) and N is still the number of $atoms/cm^2$ of absorbing material in C^{**}. Thus in the subtraction to obtain the $\bar{p}$-nucleon cross sections, the error made would be zero if there are equal thicknesses in $atoms/cm^2$ in the D_2O, H_2O, and O_2. This is easily seen from the formula for $\sigma_{\bar{p}p}$:

$$\sigma_{\bar{p}p} = \frac{1}{N_{D_2O}} \ell n \left(\frac{I_0}{I}\right)_{D_2O}\left(\frac{I'}{I'_0}\right) - \frac{1}{N_{H_2O}} \ell n\left(\frac{I_0}{I}\right)_{H_2O}\left(\frac{I'}{I'_0}\right)$$

$$= \left(\frac{1}{N} \ell n \frac{I_0}{I}\right)_{D_2O} - \left(\frac{1}{N} \ell n \frac{I_0}{I}\right)_{H_2O} + \left(\frac{1}{N_{D_2O}} - \frac{1}{N_{H_2O}}\right) \ell n \frac{I'}{I'_0} \quad (20)$$

This is very nearly the case for the D_2O-H_2O subtraction where $N_{D_2O} = 0.910 \times 10^{24}$ atoms/cm^2 and $N_{H_2O} = 0.915$ atoms/cm^2. The error is slightly larger, but still negligible, in the case of the H_2O-O_2 subtraction where $N_{O_2} = 1.170$ atoms/cm^2, especially if one remembers that because there is only about 0.5 gm/cm^2 of copper equivalent in the beam to produce this background effect, $\ell n\ (I_0/I)$ is very nearly zero anyway.

Finally, the cut-off angles, θ_c, were chosen large enough so that the measured cross sections are not influenced by the presence of either diffraction scattering or multiple Coulomb scattering.

The estimated error in the $\bar{p}$–nucleon cross sections due to the effects discussed above (except the statistical and extrapolation errors) is ± 1% and is not included in any of the tabulated figures.

3. Shielding Corrections

The $\bar{p}n$ cross sections obtained as above from a D_2O-H_2O subtraction do not represent the free neutron cross sections. This is because of a shielding of the neutron by the proton in the deuteron so that the measured cross sections are too low. Glauber[11] has calculated the magnitude of the correction to the proton-neutron cross section for this shielding effect, and this correction can be applied to our antiproton results. The corrected cross sections for antiprotons on neutrons, $\sigma_{\bar{p}n}^{corr}(\theta_c)$ and $\sigma_{\bar{p}n}^{corr}(\theta_c)$, is given in terms of the $\bar{p}p$ cross sections:

$$\sigma_{\bar{p}n}^{corr}(\theta_c) = \left[\frac{1}{1-c\sigma_{\bar{p}p}(\theta_c)}\right] \text{"}\sigma_{\bar{p}n}\text{"}(\theta_c) \quad (21)$$

$$\sigma_{\bar{p}n}^{corr}(an) = \left[\frac{1}{1 - c\sigma_{\bar{p}n}(an)}\right] \text{"}\sigma_{\bar{p}n}\text{"}(an) \qquad (22)$$

The constant c is given by $\langle \text{"}r^{-2}\text{"} \rangle_d / 2\pi$, where r is the distance between the neutron and the proton in the deuteron, and the brackets denote expectation value. This function, which behaves asymptotically for large neutron-proton separation as $1/r^2$, remains finite for small r; however, its form is not well known at small r. Therefore, c is evaluated from proton cross section data,[8] and has the approximate value 7.32×10^{-3} mb^{-1}. Inserting the experimental values for $\sigma_{\bar{p}p}(14^\circ)$, $\sigma_{\bar{p}p}(20^\circ)$, and $\sigma_{\bar{p}p}(an)$ of 104, 102 and 89 mb, respectively, we obtain correction factors of 4.2, 3.95, and 2.87, respectively. These correction factors are extremely large, and almost certainly incorrect for reasons discussed below. A similar correction must be made to the pn measured cross sections. The correction factor is 1.10--much smaller in this case because $\sigma_{\bar{p}p}$ is replaced by the much smaller σ_{pp}. This experiment did not measure σ_{pp} (inel.); hence, the correction factor for σ_{pn} was taken from Chen et al.[8]

The shielding correction for antiprotons is uncertain in several respects. First, the deuteron wave function at small distances is not well known. Second, in the calculation of the shielding effect (Eq. 21 and 22) it was necessary to assume a "black-sphere" model for the nucleons. In the light of our large annihilation cross sections compared with the total cross section, this assumption is probably reasonable. Third, however, it was also necessary to assume that the neutron-proton separations in the deuteron are much larger than the interaction range of the incident particle.[11] Our large $\bar{p}p$ cross section (104 mb) implies a range of interaction of about $\sqrt{104 \times 10^{-27} \text{ cm}^2/\pi}$, or 1.8×10^{-13} cm. This range probably cannot be considered small enough to justify this assumption. The above correction, which is valid for small interaction ranges, deviates widely from the correct function when the radius of the deuteron is smaller than the range of interaction (see especially Fig. 1 of ref. 11). Because of the large range of interaction of the antiproton,

we must use the more general formulas of Glauber (Eq. 20 and 22 of Ref. 11) to calculate the correction to the cross sections. In practice, we used the data of Fig. 1 of Glauber with an interaction range of 1.8×10^{-13} cm, and the Hulthén wave function to numerically integrate his Eq. 22. The result is that our measured cross sections must be increased by about 37 mb.

Blair[12] has calculated the deuteron shielding effect on the antiproton-neutron cross sections in the impulse approximation assuming the Hulthén wave function for the deuteron, but without assuming a small range for the antiproton-nucleon interaction. This correction is, therefore, probably more reliable than the Glauber correction as given above, although it still suffers from the assumption that the antiproton-nucleon interaction can be represented by a black absorbing disk. Blair presents his results in the form of plots of $\sigma_{\bar{p}n}$(true) - $\sigma_{\bar{p}n}$(apparent=measured) versus $\sigma_{\bar{p}n}$(apparent) for several values of $\sigma_{\bar{p}p}$. Again we use $\sigma_{\bar{p}p}(\theta_c)$ to evaluate $\sigma_{\bar{p}n}^{\text{true}}(\theta_c)$ and $\sigma_{\bar{p}p}$(an) to obtain $\sigma_{\bar{p}n}^{\text{true}}$(an). The resulting "true" values are given by: $\sigma_{\bar{p}n}^{\text{true}}(\theta_c) = \sigma_{\bar{p}n}^{\text{meas}}(\theta_c) + 38$ mb so that $\sigma_{\bar{p}n}^{\text{true}}(14^o) = \sigma_{\bar{p}n}^{\text{true}}(20^o) = 108$ mb and $\sigma_{\bar{p}n}^{\text{true}}(\text{an}) = \sigma_{\bar{p}n}^{\text{meas}}(\text{an}) + 28$ mb = 74 mb. These corrected $\bar{p}n$ cross sections are listed in Table VIII.

With this shielding correction to the $\bar{p}n$ cross sections, the cross sections for $\bar{p}p$ and $\bar{p}n$ appear to be nearly equal both in the attenuation and annihilation cross sections. It may be that $\sigma_{\bar{p}p}$(an) is lower than $\sigma_{\bar{p}p}$(an), but this has not been demonstrated statistically by the present experiment. The annihilation process for antiprotons on protons may proceed either through the isotopic spin state (I=1, I_3=0) with a cross section σ_1, or the isotopic spin state (I=0, I_3=0) with a cross section σ_0. The $\bar{p}p$ system is in each of the two isotopic spin states with equal probability. The $\bar{p}n$ system, however, exists only in the isotopic spin state (I=1, I_3=-1) and thus annihilates only with a cross section σ_1. Obviously, equal annihilation cross sections for the $\bar{p}p$ and $\bar{p}n$ systems are allowed in the isotopic spin formalism only if σ_1 is equal to σ_0. However, the accuracy of the experimental cross sections must be considerably improved before we may conclude that σ_1 is equal to σ_0.

4. Total Antiproton-Nucleon Cross Sections

At this point let us compare our results to a direct measurement of the total $\bar{p}p$ cross section recently performed at Berkeley.[4] This was a good-geometry experiment in which the total $\bar{p}p$ cross section was measured for several antiproton energies by observing the transmission of antiprotons through liquid hydrogen. No attempt was made to obtain the annihilation cross section, and a comparison with positive protons was not made. The result for 450 Mev antiprotons is 99±7 mb. Because the measurement was done with good geometry, the correction for the forward elastic scattering is small (about 2 mb), and is included in the above value. This value is only slightly higher than our total annihilation cross section, 89±7 mb and is about equal to our attenuation cross section obtained at "poor" geometry, 108±8 mb.

It is customary to obtain estimates of the total cross section by adding a correction to the measured cross section for the forward diffraction scattering into the finite (and in our case large) solid angle subtended by the pass-through counters at the target. One method is to extrapolate our two measured cross sections to zero solid angle. However, with measurements at only two angles, we would have to make a straight line extrapolation, and this assumes a constant, differential scattering cross section per unit solid angle from 0° to the largest cut-off angle used, 20.5°. This assumption would probably be quite inaccurate, as the diffraction scattering is almost certainly peaked forward. This type of extrapolation would thus give a value lower than the correct total cross section. In fact, within the statistics, we obtain the same value for the cross section for the two cut-off angles used in this experiment (14.3° and 20.5°) showing very little diffraction present at these large angles. Our measured cross sections thus represent more nearly the total inelastic cross sections for the $\bar{p}p$ and $\bar{p}n$ interactions.

Our measured cross sections show a very large probability for the annihilation of an antiproton and a nucleon. Hence, it may be reasonable, as a crude approximation, to picture the nucleon, as seen

by the antiproton as a black disk of area surrounded by a grey region of undetermined size. Then one would expect, because of the shadow scattering of the black area, that the total cross section would be at least twice the annihilation cross section. However, because the nucleon may not be entirely black to an antiproton over an area this large, one can not say specifically that the total cross section must be at least twice as large as the annihilation. This can be understood by a glance at Fig. 2.2 on page 322 of Blatt and Weisskopf,[13] which is a plot of the lower limit of the elastic scattering cross section for a given reaction (for our considerations, the annihilation) cross section. From this diagram it is seen that for the elastic scattering to be appreciably smaller than the annihilation, the nucleon must appear quite transparent to the antiproton. In this case it would be necessary to postulate a rather large grey sphere to account for the large amount of annihilation. The correct picture is probably somewhere between these two extremes and will require further experimental investigation.

A model of this form--a black region of arbitrary size surrounded by a potential--has been used by Koba and Takeda[14] to calculate annihilation and scattering cross sections for the antiproton–proton collision. These authors find that a large annihilation cross section can be obtained by postulating a sufficiently large black central region, and that the scattering cross section may be either smaller or larger than the annihilation cross section depending on the interaction potential outside this black central region. This outside potential appears not to influence greatly the annihilation cross section if it is attractive, and to reduce σ_{an} if it is repulsive.

If we assume that the antiproton annihilates with a nucleon only when they approach close enough for the cores to overlap, then we obtain a core radius of about $(1/2)\sqrt{\sigma_{an}/\pi} = (1/2)\sqrt{89 \times 10^{-27}\,\mathrm{cm}^2/\pi}$ = one-half of a "radius of annihilation" = 0.85×10^{-13} cm. This "core radius" is four times the proton Compton wavelength. This is very nearly equal to the size of the proton charge distribution measured at Stanford.[14] Because the size of the nucleon core is generally attributed

to the recoil of the nucleon upon emission of pions, the core radius should be about equal to the proton Compton wavelength (0.21×10^{-13} cm.)[15] Another suggestion of a large nucleon core has been suggested by Tamm.[16]

5. Conclusions

The inelastic cross section for 450-Mev antiprotons incident on protons is 104 ± 8 mb., and the total annihilation cross section is 89 ± 7 mb. The corresponding $\bar{p}n$ cross sections, after a correction for the shielding effects of the two nucleons in the deuteron is made, are 104 ± 9 mb, and 68 ± 10 mb. Thus the $\bar{p}p$ and $\bar{p}n$ interaction and annihilation cross sections are the same within the limits of this experiment, and annihilation is the most probable inelastic event that can befall the antiproton in collision with a nucleon.

It is difficult to reconcile these results with a recent measurement of the total $\bar{p}p$ cross section of 97 ± 4 mb at a similar energy. In particular a study of the diffraction scattering of antiprotons on nucleons would be of great interest. An important experiment along this line would be the measurement of the transmission of antiprotons through liquid hydrogen as a function of the cut-off angle defined by the pass-through counter, from the smallest angles feasible to the large angles of this experiment. This would check both the good and the poor geometry results given above, and also give information on the region between them.

F. Cross Sections for Antiprotons on Complex Nuclei

1. Formulas and Results

Because of the considerable amount of extraneous absorber in the beam (methyl alcohol in C^*) when the antiproton cross sections were measured on copper, silver, and lead, it was necessary to take data with no absorbers in the slots of C^*. To compute the relevant cross sections, we again use the formulas

$$\sigma(\theta_c) = \frac{1}{N} \ell n \frac{I_0}{I(\theta_c)} \quad \frac{I'(\theta_c)}{I'_0} , \qquad (1)$$

$$\Delta\sigma(\theta_c) = \frac{1}{N}\left\{\frac{1}{I(\theta_c)} - \frac{1}{I_0} + \frac{1}{I'(\theta_c)} - \frac{1}{I'_0}\right\}^{1/2} \qquad (2)$$

and

$$\sigma_{an} = \frac{1}{N}\,\ell n\,\frac{I_0}{I_0 - I_{an}}\,\frac{I'_0 - I'_{an}}{I'_0} \,. \qquad (3)$$

The results for antiprotons on copper, silver, and lead are shown in Table IX. Also included are the oxygen cross sections given in Table VII. Again, for the purpose of comparison, the corresponding proton cross sections were measured, both electronically and photographically, and are also included in Table IX.

The 14.3^{o} cross section for lead, for both antiprotons and protons is placed in parenthesis because it may be affected by some multiple Coulomb scattering. The value in parenthesis has been corrected for this multiple scattering as follows: If a fraction 1-F of the beam is lost by multiple scattering, the actual transmission is I/FI_0, instead of the observed I/I_0. This results in an apparent increase of $\sigma_m = (1/N)\ell nF$ in the correct cross section, where N is still the thickness of the lead absorber in atoms/cm^2. The magnitude of F is difficult to calculate because of such complicating factors as (1) a broad incident beam, (2) a divergent incident beam, and (3) nonuniform illumination of counter S3 (see Fig. 3). Sternheimer[17] has calculated F as a function of two variables r_0 and ρ_0, where ρ_0 is the radius of a uniform circular beam, which may be divergent, divided by the radius of the pass-through counter, and r_0 is a function of the experimental geometry and the rms scattering angle. Assuming a uniform beam, we obtain a value for F of 0.99, resulting in $\sigma_m = 60$ mb for the 14.3^{o} results. The correction for $\theta_c = 20.5^{o}$ is negligible, as is the multiple-Coulomb scattering correction for all other attenuators used in this series of experiments. Subtracting this σ_m value from $\sigma_{Pb}(14^{o}) = 2910 \pm 222$ mb results in $\sigma_{Pb}^{corr}(14^{o}) = 2850 \pm 225$ mb. The multiple scattering correction is the same for protons, so we must also lower

Table IX

Antiproton Interaction Cross Sections in Complex Nuclei (mb)

Element	$E_{\bar{p}}$ (Mev)	$\sigma(14^\circ)$ $\bar{p}$	p^+	$\sigma(20^\circ)$ $\bar{p}$	p^+	σ_{an} $\bar{p}$	σ_r $\bar{p}$	p^+	$\frac{\sigma_r p}{\sigma_r p^+}$	$\frac{\sigma_r p}{\sigma_{an}}$
O	457	556±10	292±2	517±10	246±2	453±9	590±12	340±4	1.74±.04	1.36±.04
Cu	411	1240±82	719±5	1220±88	640±4	1060±61	1260±91	880±10	1.44±.11	1.19±.10
Ag	431	1630±170	1052±6	1640±183	924±6	1500±157	1635±188	1170±12	1.39±.16	1.09±.17
Pb	436	2910±222 (2850±225)*	1722±22 (1662±50)*	2680±254	1461±10	2010±182	(3005±275)†	(1845±40)	(1.62±.16)	(1.49±.20)†

σ_r is the total inelastic cross section obtained by extrapolation of $\sigma(\theta_c)$ vs $2\pi(1-\cos\theta_c)$ to zero θ_c.

*corrected for multiple scattering

†see text Section F-2 for explanation of the data in parenthesis.

the $\sigma_{Pb}^{p^+}(14^o)$ from 1722 ± 2 mb to 1662 ± 50 mb. These corrected values are listed in Table IX below the directly measured values.

2. Errors

The errors given in Table IX represent standard deviations due to counting statistics compounded with the estimated error in extrapolation to zero C* pulse height as explained in Section II-E1. In the case of the 14.3° lead attenuation cross section an error of about ± 2% must be included because of the uncertainty of the multiple scattering correction. Because the thickness of the lead absorber may affect $\sigma_{Pb}(14^o)$, all quantities in Table IX involving this cross section are placed in parenthesis.

The error in the extrapolated cross section, σ_r (the inelastic cross section), is only slightly higher than the errors in the measured cross sections. This is because the measurements at 14.3° and 20.5° are not independent, and the error in the difference $[\sigma(14^o) - \sigma(20^o)]$ is quite small.

Other possible sources of error are discussed in Section II-E2 and are negligible compared to the large statistical errors.

3. Total Absorption Cross Sections

The attenuation cross sections given in Table IX are the cross sections for all interactions removing antiprotons in the incident beam from the solid angle defined by the cut-off angle θ_c. To obtain the total absorption cross section σ_r we must add the cross section for the production of secondaries other than those resulting from annihilations, which are detected in the pass-through counter but not detected in C*. These secondaries are mainly inelastically scattered charged particles and have the effect of reducing the measured cross sections even at our large cut-off angles. The total absorption cross section can be obtained from the measurements at the two poor geometries $\theta_c = 14.3^o$ and $\theta_c = 20.5^o$ by extrapolating to zero solid angle to eliminate these charged secondaries. This is done in Fig. 17 for the antiproton cross sections and in Fig. 18 for the proton cross sections. Because we have experimental cross

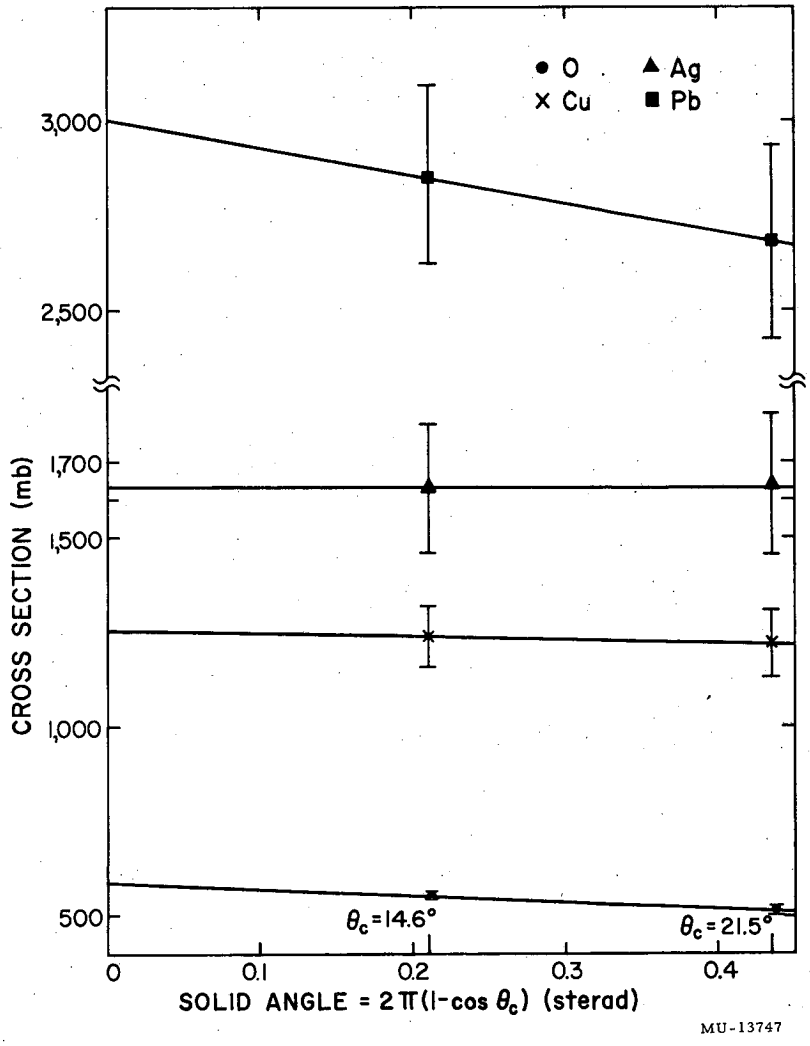


Fig. 17. Antiproton-nuclei attenuation cross sections versus included solid angle at the pass-through counter. The extrapolated value is σ_r, the total inelastic cross section.

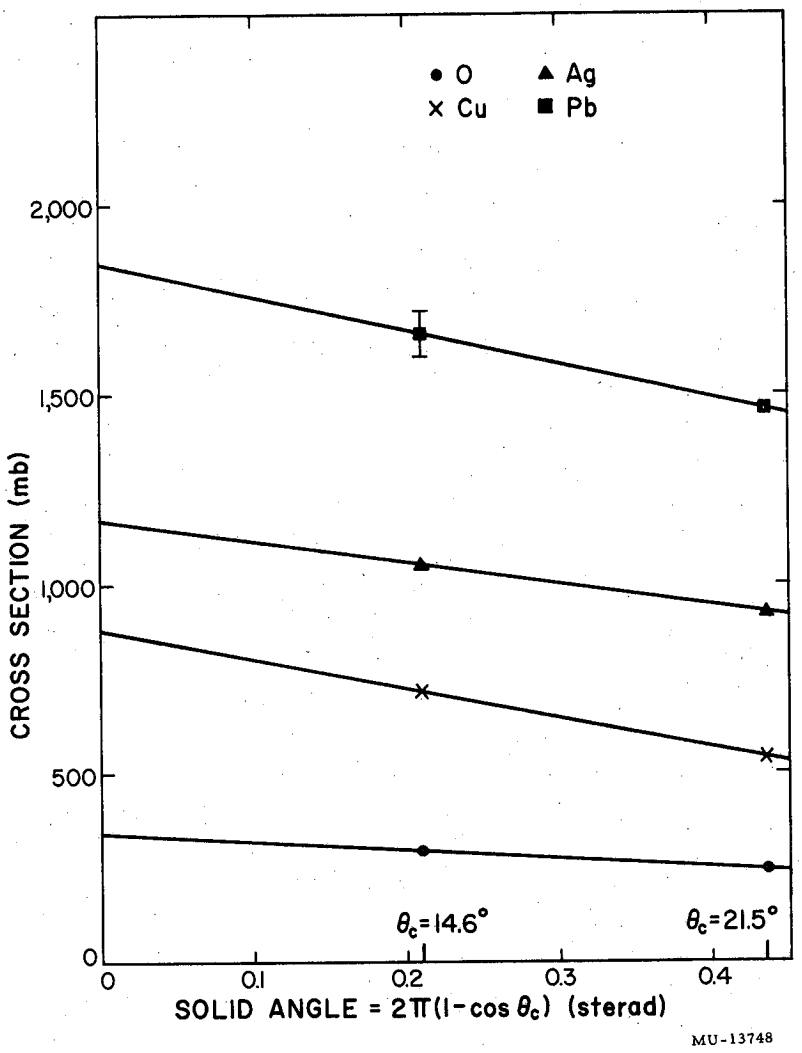


Fig. 18. Same as Fig. 17, except for positive protons.

sections for only two solid angles, we must assume a linear extrapolation. This is identical to assuming an isotropic distribution of charged secondaries in the solid angles considered. The extrapolation lines have nearly zero slope, implying very few charged secondaries, so that the effect of this assumption is probably quite small. We note that the slopes of the straight lines are much greater for the proton cross sections than for the antiproton cross sections. This is expected in view of the large annihilation cross sections for antiprotons, i.e., the most probable inelastic event that can befall the antiproton is annihilation, so the number of charged nonannihilation secondaries is relatively small, while, for the protons, the only inelastic processes are nonannihilation and, hence, will cause a greater decrease of the measured cross sections for increasing solid angle.

Table IX gives the values of σ_r obtained and also the ratio of σ_{an}/σ_r for the elements O, Cu, Ag, and Pb. It is seen that in all cases, the reaction cross section is mainly due to the annihilation process.

4. Discussion

The copper cross section for $\theta_c = 14.3^\circ$ obtained in this experiment (1240 ± 82 mb) does not disagree with the less precise value obtained for nearly the same energy antiprotons in Run I at a cut-off angle of 12° (1580 ± 220 mb). This measurement of the annihilation cross section for copper (1060 ± 61 mb) agrees well with the previous result from Run I (1050 ± 220 mb). Also, our antiproton total inelastic cross-section measurement for lead (3005 ± 275 mb) can be compared with a previous measurement (2330 ± 650).[4] Finally, our positive proton cross sections compare favorably with those obtained at Brookhaven with a similar geometry and at a somewhat higher energy.[18]

It is customary to define the radius R of the nucleus as seen by the incident particle by the equation

$$\sigma_r = \pi R^2 = \pi(a + r_0 A^{1/3})^2 \qquad (23)$$

where σ_r is the reaction cross section and r_0 is a radius parameter. In Fig. 19 we have plotted $\sqrt{\sigma_r/\pi}$ versus $A^{1/3}$ for the experimental values of σ_r for antiprotons incident on O, Cu, Ag, and Pb. These points have been fitted by the least squares method to a straight line. The slope of this line is r_0, the radius parameter. Omitting the point for lead (about which there is some doubt) the value of r_0 thus obtained is $1.29 \pm 0.08 \times 10^{-13}$ cm. Similar plots are included for the annihilation cross section for antiprotons and for the proton reaction cross sections. The results for the respective slopes are 1.29 ± 0.08 and $1.31 \pm 0.01 \times 10^{-13}$ cm, where only statistical errors have been included. The nuclear radius appears to be nearly equal with these three methods. The finite intercepts of the $\sigma_r^{\bar{p}}$ and σ_{an} curves should probably be associated with a "finite size" for the antiproton.

The ratio of the absorption (total inelastic) cross section for antiprotons to that for protons is seen to decrease from 1.75 for oxygen to only about 1.4 for silver. This may indicate that the difference between the antiproton and the proton cross sections is due to interactions of the antiprotons with nucleons near the surface of the nucleus. The larger the nucleus, the more the effect of the surface is "washed out". This is because the diffuse edge of the nucleus has approximately the same thickness for all nuclei (with $Z \gtrsim 6$), [19] and therefore its area increases roughly as the nuclear radius, while the area of the central region of the nucleus increases much faster (as the square of the radius).

To understand this surface effect of the nucleus, let us consider a "radius of interaction" for the antiproton-proton interaction. This is permissible because the wavelength of the interacting particles is smaller than the "radius of interaction". This radius is obtained (see Section II-E4) from $\sqrt{\sigma_t/\pi}$. In view of the uncertainties in obtaining a value for σ_t from our measured cross sections, we will instead consider a "radius of annihilation" for the $\bar{p}$-nucleon system. Because of the closeness of the two cross sections, $\sigma_{\bar{p}p}(an) = 89 \pm 7$ mb and $\sigma_{\bar{p}n}(an) = 78 \pm 8$ mb, we consider only $\sigma_{\bar{p}p}(an)$ and set $r_{an} = \sqrt{89 \times 10^{-27}\,\text{cm}^2/\pi}$, where now r_{an} is our "radius of annihilation". We find $r_{an} = 1.68 \times 10^{-13}$ cm,

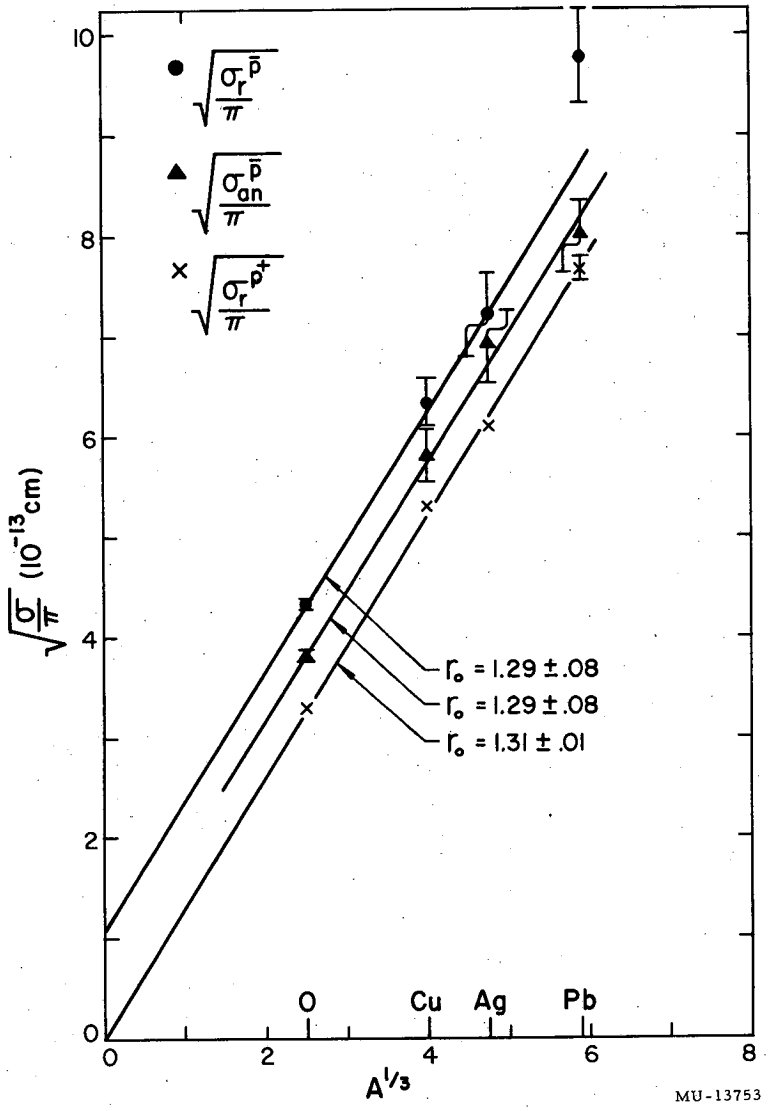


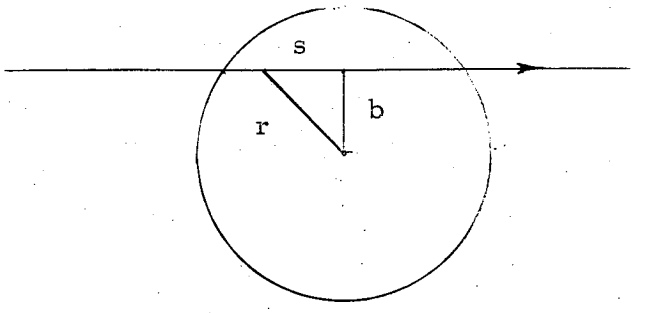
Fig. 19. Plot of $A^{1/3}$ versus $\sqrt{\sigma/\pi}$ for the three cross sections $\sigma_r^{\bar{p}}$, $\sigma_{an}^{\bar{p}}$, and $\sigma_r^{p^+}$.

and we would expect an antiproton and a nucleon to annihilate when they approach to within this distance. This is the same magnitude as the internucleon spacing at the center of nuclei, and, hence, explains the nearly complete opacity of the nucleus for antiprotons. Because this "annihilation radius" is much larger than the radius of interaction of the proton-nucleon system $\cong \sigma_{pp}/\pi = 0.89 \times 10^{-13}$cm, we expect the diffuse surface of the nucleus, where the density of nucleons is small, to interact more strongly with antiprotons than with protons.

6. Optical-Model Interpetation

In the optical model, the antiproton inelastic cross section, σ_r, is related to an average antiproton-nucleon cross section, $\bar{\sigma}$, and to the density of nucleons, $\rho(r)$ (where ρ is a function of the distance from the center of the nucleus). For σ_r to be a function of $\bar{\sigma}$, both the wavelength of the incident particle and the antinucleon-nucleon range of interaction should be smaller than the internucleon separation. As discussed above the latter condition does not apply in the central region of the nucleus, and we expect this region to be opaque to antiprotons. However, it is the outer edge of the nucleus that we expect to be important in the determination of the reaction cross section for antiprotons, and in this region the nucleon density decreases so that the condition is more nearly fulfilled.

The formula for the reaction cross section, σ_r, can be easily derived following the method of Fernbach, Serber, and Taylor.[20] As the incident particle wave passes through the nucleus, it is exponentially attenuated with an absorption coefficient $K(r)=\bar{\sigma}\rho(r)$. The density distribution $\rho(r)$ expresses the size and shape of the nucleus. The total attenuation is obtained from an integral of $K(r)$ along the antiproton path, s, through the nucleus at an impact paramenter b. The total inelastic, or reaction, cross section is then the probability of interaction integrated over this impact parameter b. From the accompanying sketch, we see that $r^2 = s^2 + b^2$, and therefore:



$$\sigma_r = 2\pi \int_0^\infty \{ 1-\exp\left[- \int_{-\infty}^{\infty} K\left((s^2+b^2)^{1/2} \right) ds \right] \} \, bdb \qquad (24)$$

In order to evaluate this integral and obtain a value for σ_r, we must first choose an appropriate nucleon density distribution $\rho(r)$. Because σ_r is only a function of $\rho(r)$ and $\overline{\sigma}$, the hope is that for an assumed $\rho(r)$, our measured values of σ_r will determine an average antiproton-nucleon cross section that can be compared to the experimental values. Commonly chosen density distributions are[21]

(1) a uniform density
$$\rho(r) = \rho_1 \quad r \leq R \qquad (25)$$
$$= 0 \quad r > R,$$

(2) a modified Gaussian density
$$\rho(r) = \rho_2 / \{ \exp [(r^2 - c^2)/Z_1^2] + 1 \}, \qquad (26)$$

and (3) a Fermi density
$$\rho(r) = \rho_3 / \{ \exp[(r-c)/Z_2] + 1 \}. \qquad (27)$$

The uniform density is generally considered only a first approximation, while the Fermi distribution gives the best agreement with the shape of the charge distribution for the nucleus as obtained in the Stanford electron-scattering experiments.[19]

Calculations of σ_r made as described above yield values that are too low for all of the above density distributions and for any reasonable values of $\overline{\sigma}$. The reason for this is that we have neglected the effect of the finite range of the force acting between the antiproton and the nucleon. The effect of this finite range is to spread out the effective density distribution (making the nuclear surface somewhat more diffuse) and thus to increase the calculated cross sections.

By assuming a Gaussian form for the Fermi density distribution at large distances from the center of the nucleus, Drell[22] has been able to obtain a formula for the ratio of σ_r of antiprotons on nuclei to σ_r for protons on nuclei:

$$\frac{\sigma_r^{\bar{p}}}{\sigma_r^{p^+}} = 1 + \frac{a}{A^{1/3}} \ln \frac{\bar{\sigma}_{\bar{p}\text{-nucleon}}}{\bar{\sigma}_{p^+\text{-nucleon}}}$$

where a is a constant depending on the shape of the Gaussian used. This formula gives fairly good agreement with our measured reaction cross sections for values of $\bar{\sigma}_{\bar{p}\text{-nucleon}}$ of about 150 mb. However, we note that the value of σ_r is not a very sensitive function of $\bar{\sigma}$.

Goldhaber[23] has been able to include the effect of a finite range by using a Woods-Saxon potential to represent the nucleus. He finds that our large reaction cross sections are obtainable by this method.

Perhaps a more straightforward method of including the effect of the finite range of the antiproton-nucleon interaction is the method proposed by Williams.[24] If we assume only two-body interactions, each nucleon of the nucleus will contribute to the absorption coefficient K an amount that is proportional to the elementary cross section $\bar{\sigma}$, and which is a function F of the distance between this nucleon and the incident antiproton. Thus the i^{th} nucleon contributes $K_i(|\vec{r}-\vec{r}_i|) = \bar{\sigma} F(|\vec{r}-\vec{r}_i|)$, and the total contribution from all nucleons, obtained by summing, is $K(r) = \sum_i \bar{\sigma} F(|\vec{r}-\vec{r}_i|)$ or passing to an average over the positions of the nucleons in the nucleus:

$$K(r) = \int \bar{\sigma} F(|\vec{r}-\vec{r}'|) \rho(r') d^3\vec{r}' = \bar{\sigma} \rho_e(r) \qquad (28)$$

where $\rho_e(r) = \int F \rho d^3\vec{r}'$ is an "effective" nucleon density, and $\rho(r)$ is the actual density of nucleons in the nucleus. In order that we have $\int \rho_e d^3r = A$, F must be normalized according to $\int F(x) d^3x = 1$.

The antiproton experiments did not yield any information on the form of the density distribution $\rho(r)$. For the purpose of evaluating Eq. 24, we will therefore use the smoothed, uniform Fermi distribution which best fits the nuclear charge distributions obtained from electron scattering

experiments by Hofstadter at Stanford.[19] This form of the charge density is given by

$$\rho(r) = \frac{\rho_0}{\exp\left[\frac{r-c}{Z_1}\right] + 1} \qquad (29)$$

and describes all nuclei by a uniform central charge density which falls off smoothly at the edge. In this distribution, c is the radius parameter equal to $1.08\ A^{1/3}$, and $Z_1 = t/4.40$, where t is the surface thickness-the distance in which the density falls from 90% to 10% of its central value--and is essentially constant for all nuclei with $Z \geq 6$ with the value $t = \Delta r_{90-10} = 2.4 \times 10^{-13}$ cm. We will assume that the nucleon density distribution has the same shape and size as this charge distribution with the single exception of the parameter ρ_0 which is easily evaluated from $\int \rho(r) d^3r = A$ = the number of nucleons in the nucleus.

For the functional dependence of the antiproton-nucleon interaction, F, we have chosen a simple square-well:

$$F = \begin{cases} \dfrac{3}{4\pi r_0^3} & r < r_0 \\ 0 & r \geq r_0 \end{cases} \qquad (30)$$

The square-well range r_0 was calculated from the experimentally measured antiproton-nucleon cross section

$$\left(r_0 = \sqrt{\frac{\bar{\sigma}}{\pi}} = \sqrt{\frac{10.5 \times 10^{-26}\,\mathrm{cm}^2}{\pi}} = 1.8 \times 10^{-13}\,\mathrm{cm}\right).$$

The first step in the calculation was the numerical integration of the formula for the effective nucleon density distribution $\rho_e(r)$ using Eq. 28. The numerical integration was carried out on an IBM-650 data processing machine. Figure 20 shows as an example of the resulting effective density distributions the curve obtained for the silver nucleus together with the unmodified Fermi density distribution. It is seen that the Fermi density is only slightly modified by the square-well interaction.

experiments by Hofstadter at Stanford.[19] This form of the charge density is given by

$$\rho(r) = \frac{\rho_0}{\exp\left[\frac{r-c}{Z_1}\right] + 1} \tag{29}$$

and describes all nuclei by a uniform central charge density which falls off smoothly at the edge. In this distribution, c is the radius parameter equal to $1.08\ A^{1/3}$, and $Z_1 = t/4.40$, where t is the surface thickness-the distance in which the density falls from 90% to 10% of its central value--and is essentially constant for all nuclei with $Z \geq 6$ with the value $t = \Delta r_{90-10} = 2.4 \times 10^{-13}$ cm. We will assume that the nucleon density distribution has the same shape and size as this charge distribution with the single exception of the parameter ρ_0 which is easily evaluated from $\int \rho(r) d^3r = A$ = the number of nucleons in the nucleus.

For the functional dependence of the antiproton-nucleon interaction, F, we have chosen a simple square-well:

$$F = \begin{cases} \dfrac{3}{4\pi\, r_0^3} & r < r_0 \\ 0 & r \geq r_0 \end{cases} \tag{30}$$

The square-well range r_0 was calculated from the experimentally measured antiproton-nucleon cross section

$$\left(r_0 = \sqrt{\frac{\bar{\sigma}}{\pi}} = \sqrt{\frac{10.5 \times 10^{-26}\,\mathrm{cm}^2}{\pi}} = 1.8 \times 10^{-13}\,\mathrm{cm}\right).$$

The first step in the calculation was the numerical integration of the formula for the effective nucleon density distribution $\rho_e(r)$ using Eq. 28. The numerical integration was carried out on an IBM-650 data processing machine. Figure 20 shows as an example of the resulting effective density distributions the curve obtained for the silver nucleus together with the unmodified Fermi density distribution. It is seen that the Fermi density is only slightly modified by the square-well interaction.

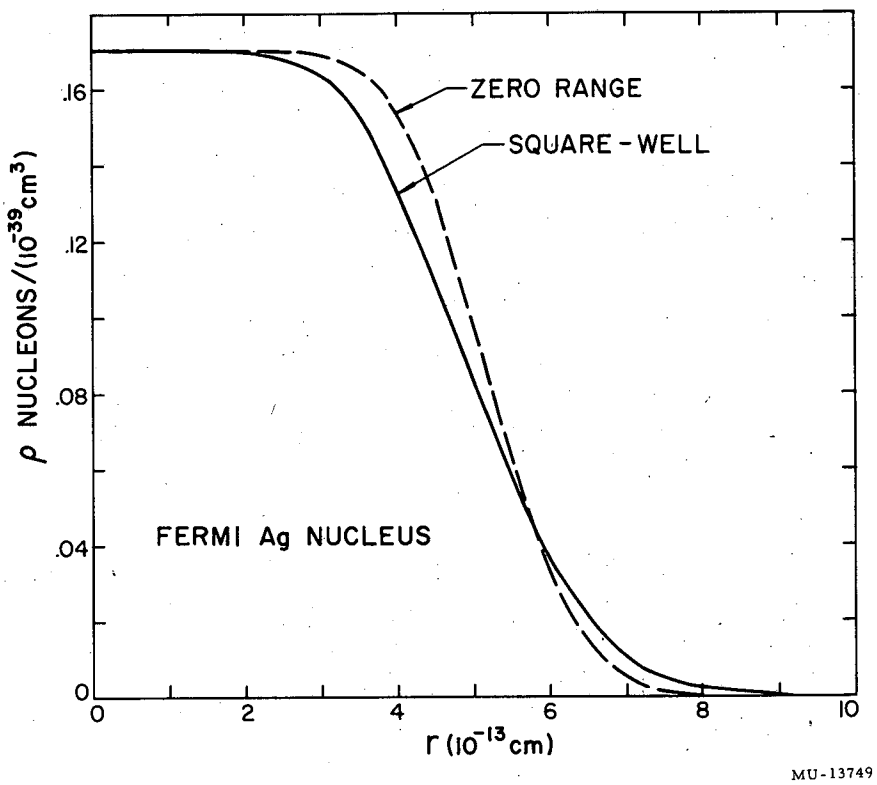


Fig. 20. Nuclear density distribution for a smoothed Fermi Ag nucleus without modification (zero-range interaction), and modified by square-well interactions.

The density distributions obtained were then inserted in Eq. 24, and the numerical integration performed to obtain the antiproton-nucleus reaction cross sections σ_r. These calculations were made for the four elements for which experimental cross sections have been obtained, oxygen, copper, silver, and lead. The calculations of σ_r evaluated for 4 values of the elementary antiproton-nucleon cross section $\bar{\sigma}$ are: 89 mb (the measured $\bar{p}p$ annihilation cross section), 105 mb (the measured $\bar{p}$-nucleon inelastic cross section), and 150 and 200 mb. The calculated values of σ_r are listed in Table X, together with the experimental reaction and annihilation cross sections. In Fig. 21 the calculated values of σ_r for $\bar{\sigma}$ = 105 mb are plotted versus $A^{1/3}$. The experimental values are also shown.

From Table X and Fig. 21 we see that the cross sections obtained from the unmodified Fermi distributions are too small, as was mentioned earlier. The values of σ_r obtained from the square-well dependence for F for an elementary cross section $\bar{\sigma}$ equal to the measured value of 105 mb are in remarkably good agreement with the experimental values of σ_r (with the exception of that for lead, where the experimental value is somewhat in doubt).

In conclusion, we remark that the calculated values of σ_r are quite insensitive to the values of $\bar{\sigma}$ employed. This is because most of the nucleons are located in the central region of the nucleus that is already black, and the entire change in σ_r must be due to those few nucleons on the surface of the nucleus. In addition, the calculated σ_r are not very sensitive to the range r_0 of a square-well antiproton-nucleon interaction for F because the density distribution is modified only slightly anyway. However, the experimental inelastic cross sections are easily obtainable by this straightforward modification of the usual optical model if we employ a square-well antiproton-nucleon interaction with a range deduced from the experimental elementary cross section.

Table X

Calculated values of the reaction (inelastic) cross sections for 4 elements based on the optical model as modified for the finite interaction range of the antiproton-nucleon system. All cross sections are in mb.

Element	Experimental Values		Zero Range				Square-Well			
	σ_r	σ_{an}	$\bar{\sigma}=89$	$\bar{\sigma}=105$	$\bar{\sigma}=150$	$\bar{\sigma}=200$	$\bar{\sigma}=89$	$\bar{\sigma}=105$	$\bar{\sigma}=150$	$\bar{\sigma}=200$
Oxygen	590±12	453±9	469	493	549	592	543	576	654	714
Copper	1260±91	1040±61	995	1029	1107	1168	1137	1181	1283	1361
Silver	1633±188	1500±157	1367	1406	1495	1565	1515	1564	1678	1765
Lead	3005±250	2010±182	1965	2012	2119	2203	2153	2209	2339	2442

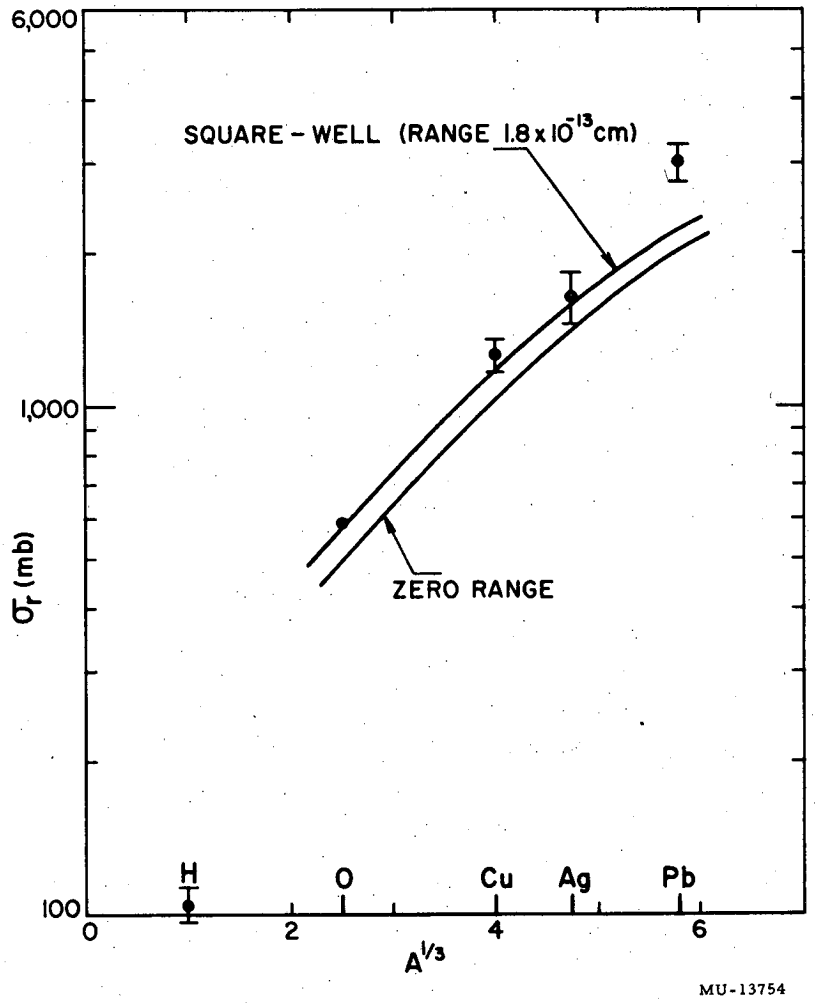


Fig. 21. σ_r versus $A^{1/3}$ for a Fermi density model modified by a square-well interaction of range r.

ACKNOWLEDGMENTS

These experiments were performed with the aid and cooperation of many persons. In particular, I would like to thank Professors Emilio Segrè and Owen Chamberlain for their continued interest and advise throughout this work. Drs. Clyde Wiegand, Thomas Ypsilantis, and Herbert Steiner contributed an enormous amount of time and effort during the entire course of these experiments. The help and guidance of all of the above persons throughout the author's graduate work at the Radiation Laboratory is gratefully acknowledged.

In addition, I would like to express my appreciation to the many members of the Segrè Group for their help on the various phases of the experiments. Thanks are due to Mr. Lewis Agnew and Mr. Ernie Rogers for their extensive work on the antiproton-selecting magnetic channel; to Dr. Ronald Mermod for his skillful design and construction of the velocity-selecting Cerenkov counters F1 and F2; and to Mr. Tommy X. G. Elioff who contributed generously his help and assistance at all times. The rapid completion of the very arduous task of film scanning was due to the efforts of, in addition to the above persons, Miss Janice Button, and Messers James Foote, Richard Weingart, and Rudolph Larson.

Finally, thanks are due to the members of the Bevatron crew under the direction of Dr. Edward Lofgren for the operation of the Bevatron.

This work was done under the auspices of the U. S. Atomic Energy Commission.

REFERENCES

1. Chamberlain, Segrè, Wiegand, and Ypsilantis, Phys. Rev. 100, 947 (1955).
2. Chamberlain, Keller, Segrè, Steiner, Wiegand, and Ypsilantis, Phys. Rev. 102, 1637 (1956).
3. Brabant, Cork, Horowitz, Moyer, Murray, Wallace, and Wenzel, Phys. Rev. 101, 498 (1956).
4. Cork. Lamberston, Piccioni, and Wenzel, "Cross Sections of Antiprotons in Hydrogen Beryllium, Carbon, and Lead." UCRL-3650, Feb. 1957 (to be published in Phys. Rev. 107, July 1 (1957)).
5. Chamberlain, Chupp, Goldhaber, Segrè, Wiegand, Amaldi, Baroni, Castagnoli, Franzinetti, and Manfredini, Phys. Rev. 101, 909 (1956), and Nuovo Cimento 3, 447 (1956).
6. Chamberlain, Chupp, Ekspong, Goldhaber, Goldhaber, Lofgren, Segrè, Wiegand, Amaldi, Baroni, Castagnoli, Franzinetti, and Manfredini, Phys. Rev. 102, 921 (1956).
7. Barkas, Birge, Chupp, Ekspong, Goldhaber, Goldhaber, Heckman, Perkins, Sandweiss, Segrè, Smith, Stork, and van Rossum, Phys. Rev. 105, 1037 (1957).
8. Chen, Leavitt, and Shapior, Phys. Rev. 103, 211 (1956).
9. V. L. Fitch, Bull Am. Phys. Soc. Ser II, Vol. I, No. 1, p. 52 (1956), invited paper.
10. O. Chamberlain and C. Wiegand, The Velocity-Selecting Cerenkov Counter, in Proceedings of the Cern Symposium on High Energy Accelerators and Pion Physics, Vol. 2 (CERN, Geneva, 1956), p. 82.
11. R. J. Glauber, Phys. Rev. 100, 242 (1955).
12. J. S. Blair, University of Washington, private communication.
13. Blatt and Weisskopf, Theoretical Nuclear Physics, (J. Wiley and Sons, New York, 1952), Ch. VIII, p. 322.
14. J. Koba and G. Takeda, Antiproton-Proton Scatterings, Oct. 1956, private communication.

15. Yennie, Levy, and Ravenhall, Rev. Mod. Phys. 29, 144 (1957).
16. I. Tamm, International Congress on Theoretical Physics, University of Washington (1956). See also footnote 38 on page 151 of Reference 14.
17. R. M. Sternheimer, Rev. Sci. Inst. 25, 1070 (1954).
18. Chen, Leavitt, and Shapior, Phys. Rev. 99, 857 (1955).
19. R. Hofstadter, Rev. Mod. Phys. 28, 214 (1956).
20. Fernback, Serber, and Taylor, Phys. Rev. 75, 1352 (1949).
21. The terminology of Hofstadter[19] is used here.
22. S. Drell, Stanford University, private communication.
23. G. Goldhaber, University of California, private communication.
24. R. W. Williams, Phys. Rev. 98, 1387 (1955).